Effects of TiN content and heat treatment on microstructural changes, mechanical strength, and corrosion resistance in selective laser melting of TiN/AISI 420 composites

Duc Tran [a], Chih-Kuang Lin [a], Pi-Cheng Tung [a], Chin-Te Lin [a], Jeng-Rong Ho [a,*], Yoshiyuki Iizuka [b], I-Yu Tsao [c], Thanh-Long Le [d]

[a] *Department of Mechanical Engineering, National Central University, Jhong-Li District, Tao-Yuan City, 32001, Taiwan*
[b] *Institute of Earth Sciences, Academia Sinica, Nangang District, Taipei, 11529, Taiwan*
[c] *Institute of Material Science and Engineering, National Central University, Jhong-Li District, Tao-Yuan City, 32001, Taiwan*
[d] *Faculty of Mechanical Engineering, Ho Chi Minh City University of Technology (HCMUT), Vietnam National University Ho Chi Minh City (VNUHCM), Ho Chi Minh City, 700000, Viet Nam*

A R T I C L E   I N F O

A B S T R A C T

This study investigates the influence of Titanium Nitride (TiN) concentration variations and heat treatment on the microstructure, strength, and corrosion resistance of TiN/AISI 420 composites fabricated via selective laser melting (SLM). Results demonstrate that the addition of TiN particles (2 μm in size) at 0.5, 1, and 2 wt percent (wt. %) to the AISI 420 alloy enhances the toughness modulus of SLM TiN/AISI 420 to 37.0 ± 1.5 J/m^3, 42.2 ± 0.4 J/m^3, and 36.2 ± 0.7 J/m^3, respectively, surpassing the SLM AISI 420's toughness of 21.3 ± 0.6 J/m^3. Moreover, a positive relationship between TiN content and corrosion resistance is observed, with 2 wt % TiN/AISI 420 composites exhibiting the highest resistance at 105.6 ± 2.5 mm/year in a 6 wt % FeCl$_3$ solution. Following heat treatment, a reduction in hardness is noted due to decreased surface residual stress and increased retained austenite. However, treated composites demonstrate improved mechanical and corrosion resistances. Particularly noteworthy is the highest toughness of 118.0 ± 1.3 J/m^3 observed in 1 wt % TiN composites and a corrosion rate of 104.7 ± 2.7 mm/year in 2 wt % TiN composites. The homogeneous dispersion of TiN particles and the phenomenon of transformation-induced plasticity significantly enhance toughness, while increased levels of retained austenite contribute to improved corrosion resistance. This work underscores the potential of advanced manufacturing techniques in developing composite materials with diverse applications, such as robotic mold inserts. It emphasizes the pivotal role of composite formulation and post-processing in augmenting material performance.

1. Introduction

Selective laser melting (SLM) represents a cutting-edge additive manufacturing (AM) technology employing high-powered lasers to selectively fuse or melt layers of powdered material, enabling the creation of intricate three-dimensional objects with exceptional precision and accuracy. Distinguished by its capability to construct parts layer by layer, SLM excels in producing custom-designed components and prototypes, offering tailored properties and intricate geometries [1]. In contrast to conventional manufacturing techniques such as casting or forging, which pose challenges in crafting small or complex structures, SLM stands out as a promising additive manufacturing method. It enables the direct production of complex-shaped parts and ensures high productivity, significantly reducing product time-to-market [2].

Martensitic stainless steels, particularly AISI 420 with multiphase microstructures, have attracted considerable attention due to their outstanding mechanical and anti-corrosion properties. Consequently, AISI 420 finds widespread application in diverse fields such as medical, aerospace, automotive, energy, molding, and tools [3]. However, SLM for AISI 420 introduces rapid solidification with high thermal gradients and solidification velocities within small melt pools. This results in the formation of columnar grains, potentially leading to challenges such as reduced ductility and property anisotropy [4]. Additionally, AISI 420 is susceptible to chloride corrosion due to its relatively modest chromium content [5]. The performance limitations are closely associated with

---

* Corresponding author.
  E-mail address: jrho@ncu.edu.tw (J.-R. Ho).

Abbreviations:

AB –	As-built	RS –	Residual Stress
AM –	Additive Manufacturing	SEM –	Scanning Electron Microscopy
CR –	Corrosion Resistance	SLM –	Selective Laser Melting
CR_t –	Corrosion Rate	TEM –	Transmission Electron Microscopy
EBSD –	Electron Backscatter Diffraction	TiN –	Titanium Nitride
EDS –	Energy X-ray Dispersive Spectroscopy	TiN-x –	mixture TiN/AISI420 powders with various x in weight percent of TiN
EL –	Elongation	TS –	Tensile Strength
HT –	Heat-treated	VED –	Volume Energy Density
HV –	Hardness	x-AB –	As-built samples
IPFs –	Inverse Pole Figures	x-HT –	Heat treated samples
RA –	Retained Austenite	XRD –	X-ray Diffraction
RD –	Relative Density	XPS –	X-ray photoelectron spectroscopy

intricate solidified microstructures, metallurgical imperfections, and residual stresses (RS) development during the AM process. Achieving exceptional mechanical properties and corrosion resistance in martensitic stainless steel produced via AM presents significant challenges despite being an important objective.

In response to the escalating demand for advanced materials exhibiting superior mechanical and chemical attributes, such as elevated hardness, strength, toughness, and corrosion resistance, a promising strategy involves the development of composites with a metal matrix reinforced by ceramic particles. The incorporation of ceramics as strengthening components within the metal matrix can augment the properties of base metals through the SLM process [6]. Numerous studies highlight that the addition of various ceramic particle types (carbides, nitrides, oxides, etc.) can enhance the properties of diverse metal matrices, including Stainless Steel, Aluminum, Titanium, Copper, High Entropy Alloys, among others [7].

Among ceramic powders, Titanium Nitride (TiN), commonly employed as a coating material in machine tools, has garnered substantial attention. Possessing exceptional thermal stability, hardness, and wear resistance, TiN has been utilized as a reinforcement in the metal matrix through SLM. Incorporating TiN particles into the metal matrix via SLM modifies its structure, thereby enhancing the mechanical and chemical properties of the raw materials. For instance, in the SLM TiN/AlSi10Mg structure, adding 2 in weight percent (wt. %) nanosized TiN particles enhances elongation, strength, and wear resistance [8]. Similarly, SLM TiN/CoCrFeNiMn samples demonstrate tensile strength and elongation values of 1036 MPa and 12 %, respectively, surpassing those of SLM CoCrFeNiMn samples [9].

Moreover, the inclusion of TiN and TiC exhibits a threefold improvement in the hardness and wear resistance of SLM TiN, TiC/Ti composite compared to pure SLM Ti [10]. Refinement of the microstructure is observed in finer and equiaxed SLM TiN/17–4SS after the addition of 2 wt % 20 nm TiN in the 17–4 stainless steel matrix, leading to a significant increase in strength and ductility [11]. The refinement of grain not only eliminated the anisotropy properties but also enhanced the strength-ductility, resulting in 860 MPa for tensile strength and 48 % for elongation [12]. Therefore, utilizing the SLM process for metal matrix composites with TiN reinforcement holds great promise for producing high-quality products with complex shapes and superior properties.

The SLM technique employs a sophisticated thermal treatment process that sets it apart from traditional casting and forging methods [13]. Various heat processing routes lead to diverse outcomes in the final SLM products [8,11]. Heat treatment can mitigate anisotropy by homogenizing the microstructure and redistributing residual stresses. The overall impact of heat during the SLM process on mechanical strength is a delicate balance between enhancing strength through precipitation strengthening and potentially reducing strength through grain boundary

strengthening, solid solution strengthening, and dislocation strengthening [14]. Notably, post-heat treatment significantly enhances the tensile strength and elongation properties of SLM AISI 420 samples [3, 15].

Moreover, there has been a growing interest in SLM TiN/AISI 420 in recent times. Zhao et al. [16] emphasized the influence of laser power on the densification of their SLM samples, achieving a remarkable value of 98.2 % at 180 W. Through the incorporation of 1 wt % TiN, they demonstrated a significant enhancement in hardness, reaching 56.7 HRC, along with a noticeable improvement in wear resistance. Our previous studies, conducted in June 2023 and January 2024, also highlighted the significant influence of volume energy density (VED) from laser processing on the surface texture, density, and hardness of SLM-produced TiN/AISI 420 materials. Incorporating 1 wt % of TiN micro-powder into the AISI 420 base significantly enhanced its hardness, tensile strength, and corrosion resistance when compared with the SLM AISI 420 samples [17,18]. To date, research concerning SLM TiN/AISI 420 is quite limited, particularly regarding the effects of TiN content and heat treatment on microstructure, mechanical properties, and corrosion resistance behavior.

In this research endeavor, our primary goal is to investigate the influence of varying TiN content and a heat treatment protocol (subjecting the material to 400 °C for 1 h, followed by tempering at 200 °C for 2 h) to examine changes in the microstructure, particularly those relevant to mechanical properties and corrosion resistance. We utilize a range of advanced techniques to facilitate a comprehensive structural analysis. X-ray diffraction (XRD) analysis is crucial in identifying the phase composition precisely. Meanwhile, scanning electron microscopy (SEM), electron backscatter diffraction (EBSD), transmission electron microscope (TEM), and energy dispersive spectroscopy (EDS) contribute by providing detailed insights into the intricacies of the microstructure. Additionally, we examine residual stress using synchrotron XRD. Furthermore, we conduct rigorous tensile tests to assess mechanical properties, while corrosion resistance is meticulously evaluated through exposure to a $FeCl_3$ environment maintained at 50 °C for 48 h. These integrated methodologies collectively enhance our ability to gain a comprehensive understanding of the characteristics and overall performance of SLM TiN/AISI 420.

2. Experimental procedure

Fig. 1 illustrates the experimental methodology utilized in this research. The process begins with the mixing of various TiN/AISI 420 composite powders derived from the initial materials, comprising TiN and AISI 420 particles. Subsequently, the selective laser melting (SLM) technique is employed to fabricate the as-built (AB) samples. Post-SLM processing treatments are then applied, yielding the heat-treated (HT) samples. Comprehensive analysis of both AB and HT samples is
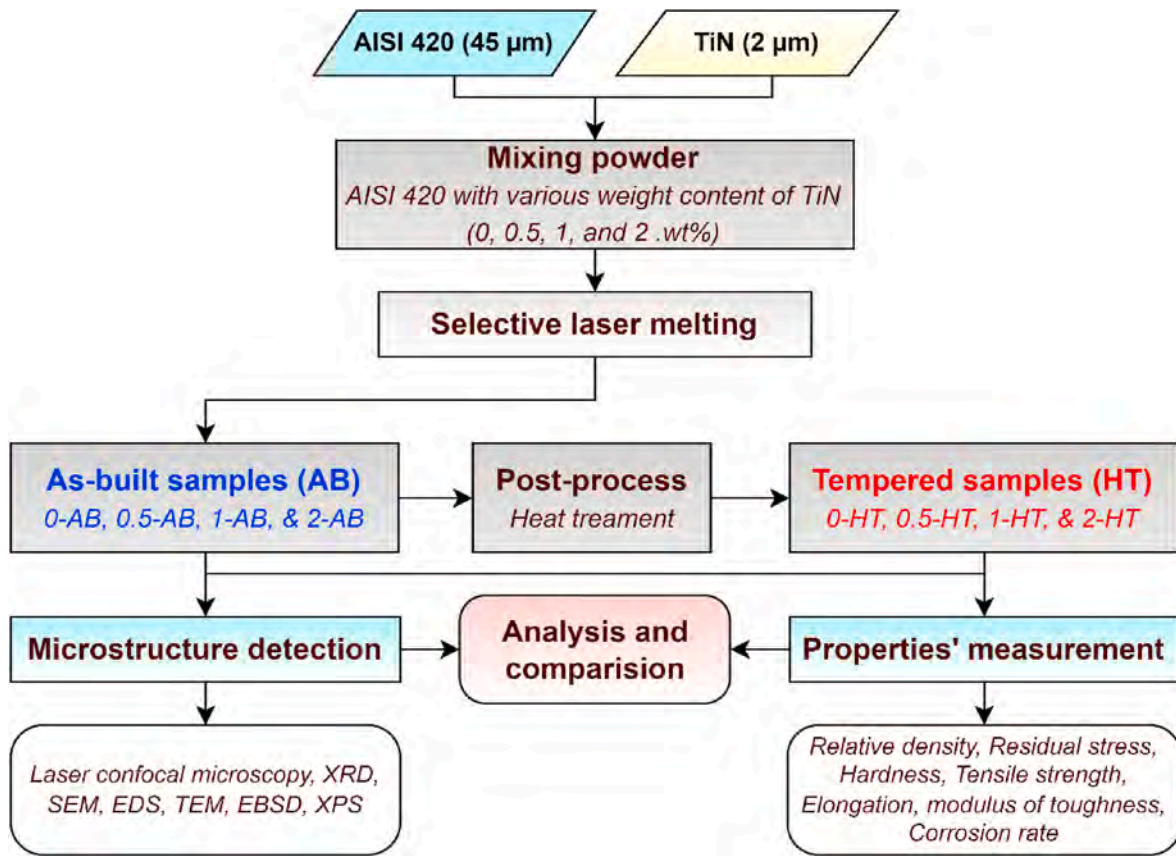
Fig. 1. Flowchart illustrating the workflow of this study.

conducted to assess their microstructure, mechanical properties, and corrosion resistance. Further elaboration on these steps is provided below.

2.1. Materials preparation

Polygonal TiN powder, sourced from Weilei Co., with an average size of 2 μm, incorporating nanoparticles (as observed in the SEM figure and particle distribution in Fig. 2a), and gas-atomized spherical AISI 420 stainless steel powder, supplied by Sanyo Co., Japan, with an average
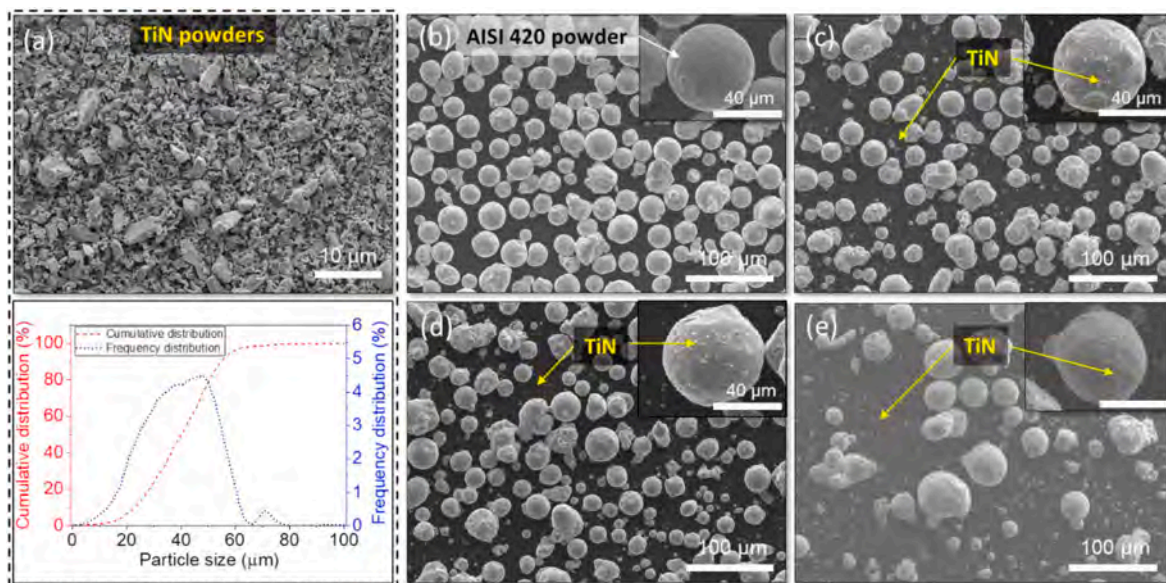

Fig. 2. (a) Illustrates the SEM images and the particle size distribution of the initial TiN powder, (b) shows the SEM images of the initial AISI 420 powder, and (c)–(e) indicate SEM images of the mixture powders with various in weight percent of TiN: (c) x = 0.5 (referred to as TiN–0.5), (d) x = 1 (referred to as TiN–1), and (e) x = 2 (referred to as TiN–2).

size of 45 µm (as shown in Fig. 2b) were utilized as the initial powders. The chemical composition in weight percent of the AISI 420 powder was 13.09 Cr, 0.49 Si, 0.34 Mn, 0.33 C, 0.06 Ni, and the balance Fe. The TiN composition consisted of 22.3 N, 1.1 O, 0.11 C, 0.03 Ni, and 0.01 Mn, with the remaining composition being Ti. To investigate the impact of TiN inclusion on the microstructure, mechanical, and corrosion properties of the SLM TiN/AISI 420 composites, various mixtures were meticulously prepared via a hybrid mixing technique [18] from x wt. % of TiN and (100 - x) wt. % of AISI 420 powders. The x–TiN/AISI 420 mixtured powders with x = 0 wt %, 0.5 wt %, 1 wt %, and 2 wt % were labeled as TiN–0, TiN–0.5, TiN–1, and TiN–2, respectively. Great care was taken to avoid agglomerations or contamination during the preparation of TiN-x powders. Following the mixing procedure, the amalgamation underwent sieving and was subsequently subjected to a reheating process at 120 °C for 2 h before commencing the printing procedure. The morphological attributes of the powders are visually depicted in Fig. 2c–e.

2.2. Selective laser melting processing

The TiN/AISI 420 samples were printed by a TONGTAI-AMP160 printer equipped with a continuous single fiber laser with a maximum output of 500 W. During manufacturing, the printer chamber was automatically sealed with nitrogen gas to prevent atmospheric exposure and maintain oxygen levels below 500 ppm. The structure of the SLM machine is presented in Fig. 3a. In addition, a scanning strategy of a rotating 67° of 1 mm stripe size is shown in Fig. 3b.

Two types of SLM samples were manufactured: (i) the cuboid samples with dimensions of $10 \times 10 \times 5$ (mm^3) for RD measurement, microstructure characterization, Vicker hardness test, and corrosion resistance test; and (ii) the dog-bone sample with dimension of gauge section were of 32 mm in length, 6 mm in width and 3 mm in thickness following ASTM E8 [19] standard for tensile test. All SLM samples were printed at a consistent VED of 168 J/mm^3, with a laser power of 280 W, laser scanning speed of 370 mm/s, a hatching distance of 90 µm, and a layer thickness of 50 µm. After printing, all samples were removed from the substrate by wire electrical discharge machining.

2.3. Heat treatment

The subsequent heat treatment was applied to the as-built samples of TiN–0, TiN–0.5, TiN–1, and TiN–2, denoted as 0–AB, 0.5–AB, 1–AB, and 2–AB, respectively. This treatment involved two cycles, each comprising the following three steps: (i) a heating phase at 400 °C maintained for 1 h, with the heating speed of 5 °C/min; followed by (ii) a tempering phase at 200 °C held for 2 h; and concluding with (iii) a cooling phase to the ambient temperature naturally in the atmospheric environment (Fig. 3c). The tempered samples corresponding to 0–AB, 0.5–AB, 1–AB, and 2–AB were designated as 0–HT, 0.5–HT, 1–HT, and 2–HT. The primary objective of the heat treatment was to alleviate internal residual stresses. Subsequently, the microstructural attributes and mechanical properties of the as-built and tempered samples were analyzed.

2.4. Characterizations

The RD was determined using the Archimedes method under the ASTM B962 standard [20]. All samples underwent grinding with sandpaper from 80 to 2000 grit for hardness test, and XRD measurement. The hardness of SLM samples was assessed using a Vickers hardness tester (*Mitutoyo HV-221*), configured with a loading of 3 kg and a dwell time of 10 s. The average Vickers hardness value was determined at five points across different locations on top surface of all SLM samples.

Furthermore, the XRD was employed to identify phase composition and assess *RS*. A qualitative analysis of the TiN/AISI 420 samples was conducted using a machine (*Bruker D8 Advance*) with Cu-Kα radiation at a wavelength of 151.8 nm. The tube voltage and current were set at 40 kV and 200 mA, respectively. Additionally, *RS* for both SLM AB and HT samples was measured using a two-angle sin 2ψ -technique, with a diffractive plane of (110), a diffractive angle of 44.67°, and ψ ranging from −50.76 to 50.76°. The *RS* measurements were taken at the center of all samples (referring to Fig. 3) and were repeated three times to obtain the average value.

For microstructure analysis, precise polishing was carried out using diamond suspensions with particle sizes of 3 µm and 1 µm. The samples were further subjected to etching using a specialized etchant consisting of 2 wt % HF and 8 wt % HNO$_3$ to reveal the microstructure. The surface characteristics of the SLM samples were examined using a laser confocal scanning microscope (*Keyence VK–X1000*). Microstructural assessments were conducted using an SEM (*JEOL JSM 7900F*). To investigate intricate details, including dispersed features and interfaces between TiN and the AISI 420 matrix, a TEM (*JEOL, JEM–2100*) was employed. EDS (*BURKER XFlash®Detector 6060*) capabilities were utilized to gain comprehensive insights into the elemental composition of these materials. For a more detailed examination of phase composition and grain morphologies, an additional set of samples underwent a refined polishing procedure employing a polisher machine (*Buehler Vibromet 2*) with a 0.02 µm silica suspension, subjected to a 48-h vibration-polishing duration. EBSD investigations were conducted using a field-emission scanning electron microscope (*FESEM, Jeol JSM-7800F Prime FEG*) outfitted with an EBSD detector. The acquired EBSD data underwent subsequent analysis employing the MATLAB open-source toolbox "MTEX." The corrosive samples underwent additional analysis using X-ray photoelectron spectroscopy (XPS, Thermo VG-Scientific/Sigma Probe instrument) to examine their surface element types and valences.

Additionally, the tensile test was conducted on a commercial servo-hydraulic mechanical testing machine (*MTS 810, USA*), following the ASTM E8-E8M standard [19]. Three trials were performed for each condition to ensure the consistency of tensile data. The ultimate tensile strength and elongation at the maximum load, along with the yield strength and toughness, were measured from the stress-strain curves.
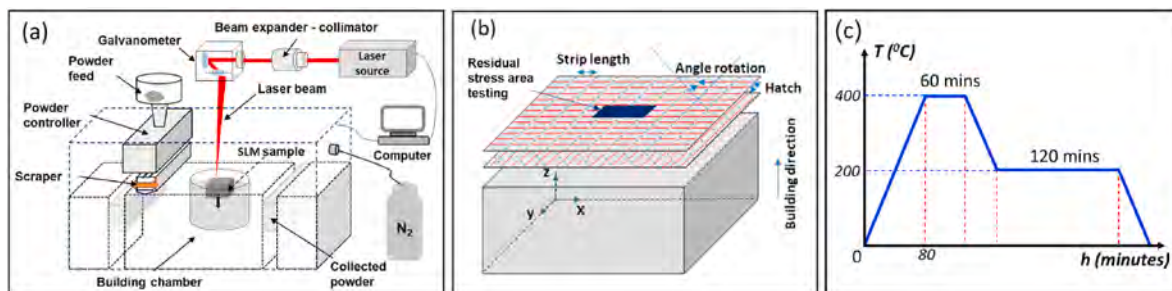

Fig. 3. Illustrates (a) the configuration of the Tong Tai-AMP 160 printer, (b) the scan strategy employed in this investigation along with the designated region for residual stress testing highlighted in red, and (c) the heat treatment cycles applied in this study for all AB samples. (For interpretation of the references to color in this figure legend, the reader is referred to the Web version of this article.)

Subsequently, SEM imaging was employed for fractography analysis.

For corrosion resistance testing, epoxy resin was used to seal all cubic AB and HT specimens, with the upper surface polished using a 1 μm diamond suspension finish. The weight loss assessment involved immersing the samples in a 6 wt% ferric chloride ($FeCl_3·6H_2O$) solution at 50 ± 5 °C for 48 h. At intervals of 12 h, the sample's mass was carefully measured using an electronic balance with a precision of 0.001 g. The corrosion rate (CR_t) was calculated using the equation $CR_t = 86.7 \times \frac{W}{D•A•T}$ [21], where W is the weight loss (g), D is the sample density (g/cm^3), A is the corrosive surface area (cm^2), and T is the corroded time (*hours*). This entire procedure was repeated three times, each with distinct sets of samples.

3. Results

3.1. Relative density, surface morphological, and phase identification

The RD values of both AB and HT samples are presented in Fig. 4a. It is observed that all RD values exceed 99 %, suggesting that high-quality samples were produced via the SLM process. Notably, sample 0-AB demonstrated the highest at 99.5 ± 0.14 %. Interestingly, with an increase in TiN content to 0.5 wt%, 1 wt%, and 2 wt%, the RD values for 0.5–AB, 1–AB, and 2–AB samples decreased to 99.45 ± 0.21 %, 99.41 ± 0.16 %, and 99.22 ± 0.15 %, respectively. The decrease in RD with an increase in TiN content in the mixture suggested that the TiN content affects: i) the laser absorption of the mixture powder and ii) molten morphologies [11]. Detailed explanations will be presented in Section 4.1. Furthermore, all the RD values for the HT samples showed a slight increase compared to their AB counterparts, measuring 99.60 ± 0.12 %, 99.53 ± 0.18 %, 99.35 ± 0.22 %, and 99.24 ± 0.17 % for 0–HT, 0.5–HT, 1–HT, and 2–HT, respectively. Heat treatment facilitated the shrinkage or closure of existing pores in the SLM samples, pivotal for augmenting the density. The thermal cycle employed during heat treatment aided the diffusion process, enabling atoms to migrate and occupy voids, further consolidating the material's structure [22].

Surface examination was undertaken on both AB and HT specimens, as demonstrated in Fig. 5. Optical imagery, presented in Fig. 5a–h, the polished surface of all SLM samples, both in AB and HT states, observed to be smooth, displaying no signs of inadequate infusion or prominent pores. This observation indicates a superior relative density value (above 99 % in all cases), a finding corroborated by Fig. 4a. A closer inspection reveals minor alterations on the AB sample surfaces compared to the HT samples. The observable decrease in small black spots on the AB surfaces points to subtle differences from their HT counterparts, highlighting the nuanced variations in surface characteristics between the AB and HT processed samples.

For a more in-depth analysis of defect formation during the SLM process, high-magnification SEM images of the AB samples were selected, as depicted in Fig. 6. The smooth surface with minimal defects observed in Fig. 6a signifies the SLM process's stability. However, introducing TiN particles into the AISI 420 matrix led to surface defects

in the SLM-processed TiN/AISI 420 samples. These defects, documented in the imagery, comprise small pores (Fig. 6b and c), TiN agglomerates, and open pores accompanied by cracks encircling the pores (Fig. 6d). Such flaws are pinpointed as the principal contributors to the diminished relative density of the TiN/AISI 420 samples in contrast with the pure SLM AISI 420 samples. These observations underscore the impact of additive materials on the surface integrity and density of SLM-manufactured parts. The ensuing sections will delve into the implications of TiN incorporation on the microstructural and mechanical properties of the SLM TiN/AISI 420 samples, highlighting its significant influence.

Fig. 7 presents the XRD spectra, including the information about phase composition of all SLM AB and HT samples. These spectra revealed a complex composition characterized by the coexistence of martensite (α-Fe) and retained austenite (γ-Fe). While τ-TiN (according to *JCPDS card 87–0632*) contributed a minor content that could be neglected and will be detected in the next section. A comparative analysis between Fig. 7a and b revealed the absence of any novel phases within the structure after the heat treatment. The observed minor alterations in peak intensities signified phase composition variations between the diverse AB samples and their counterparts HT samples after the tempering duration.

All examined specimens exhibited discernible crystalline patterns, with α-Fe identified as the predominant phase and subordinate contributions from auxiliary phases. These compositional alterations were accurately determined through meticulous Rietveld analysis of the samples' crystalline composition. As evident from the data in Table 1, the γ-Fe tended to decrease with an increase in the TiN content in the AISI 420 matrix. For instance, sample 0–AB exhibited 86.88 ± 0.43 % α-Fe, with γ-Fe constituting 13.12 ± 0.41 %. In comparison, the α-Fe percentages for 0.5–AB, 1–AB, and 2–AB were 97.40 ± 0.43 %, 98.33 ± 0.52 %, and 98.97 ± 0.38 %, respectively. In contrast, γ-Fe contributed lower percentages at 2.49 ± 0.17 %, 1.66 ± 0.51 %, and 0.15 ± 0.07 %. Following the HT process, the proportions of γ-Fe for 0–HT, 0.5–HT, 1–HT, and 2–HT tended to increase to 16.75 ± 0.43 %, 9.89 ± 0.38 %, 4.01 ± 0.19 %, and 0.61 ± 0.12 %, respectively. The heightened presence of γ-Fe phase transformation after HT was believed to significantly influence the hardness, mechanical properties, and corrosion resistance of the SLM samples. The expedited localized cooling inherent to SLM processes facilitated the formation of martensite phases within the material. The outcomes from the Rietveld analysis align with the results derived from EBSD, to be further elaborated upon in Section 3.3, collectively corroborating the identified phases and their distribution within the samples.

3.2. Residual stress

Fig. 4b illustrates the *RS* on the surface of both AB and HT samples. Notably, all samples exhibited tensile residual stress. The experimental data provides insights into the influence of TiN content and the HT process on *RS*, contributing to a comprehensive understanding of the
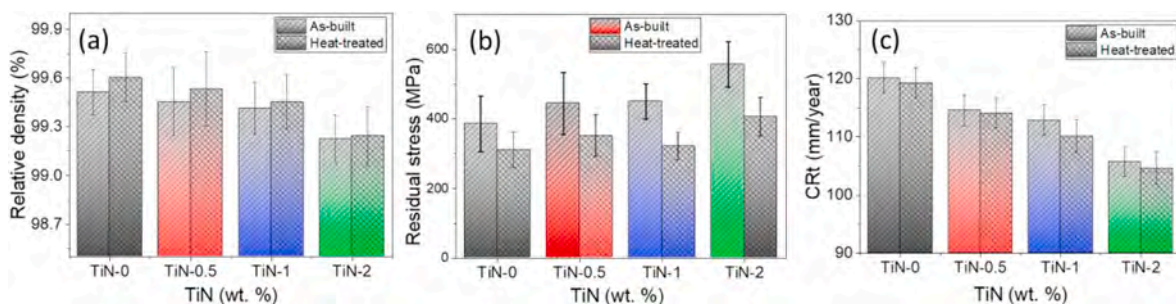

Fig. 4. Depicts (a) the relative density (RD), (b) the residual stress (RS) and (c) the corrosion rate in FeCl₃ 6 wt% after 48 h of all SLM TiN-x samples (x = 0, 0.5, 1 and 2 in wt. % of TiN) in as-built (AB) and heat treated (HT) states.
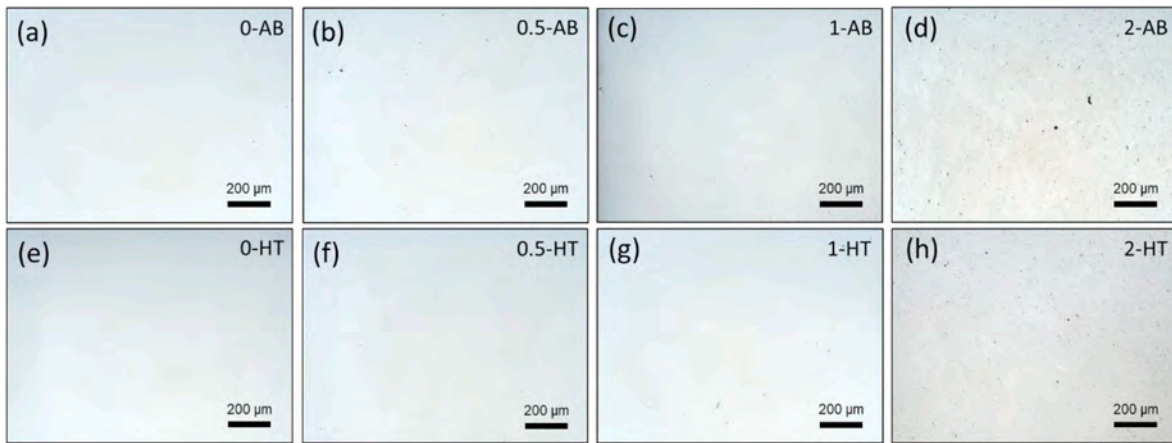
Fig. 5. Indicates the optical images of polished surface morphologies for all as-built samples: (a) 0-AB (b) 0.5–AB, (c) 1–AB, (d) 2–AB and heat treated samples: (e) 0–HT, (f) 0.5–HT, (g) 1–HT, (h) 2–HT.
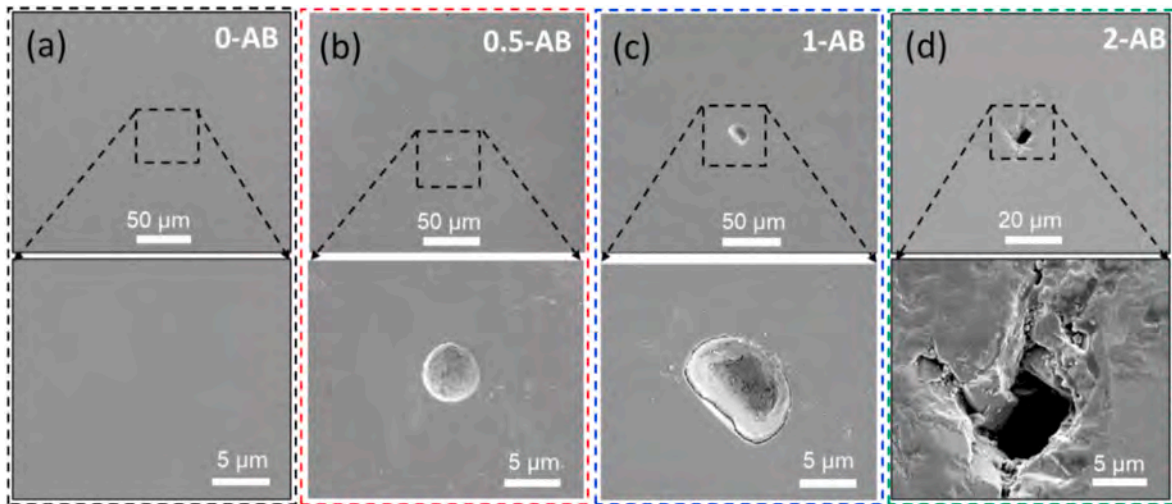

Fig. 6. Illustrates the SEM images for surface morphologies of the polished samples: (a) 0–AB, (b) 0.5–AB, (c) 1–AB, and (d) 2–AB.
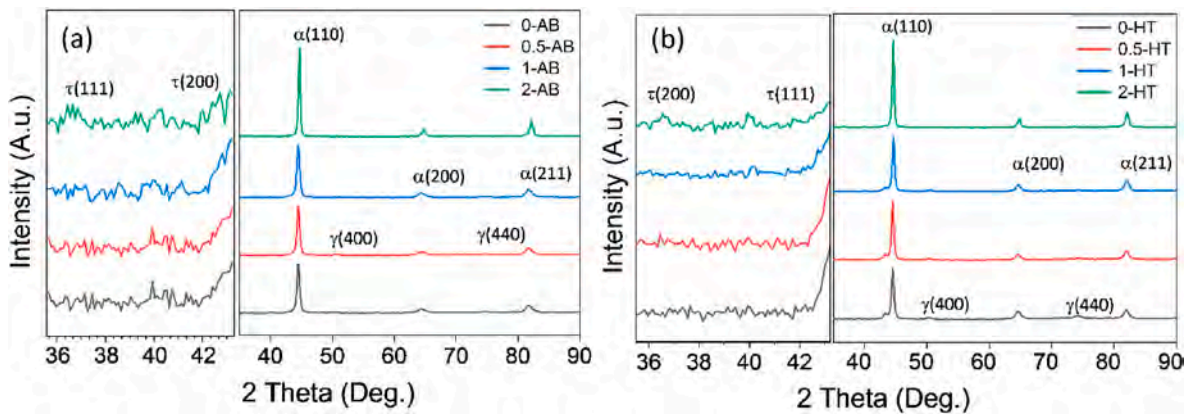

Fig. 7. Illustrates the XRD patterns of all SLM TiN/AISI 420 samples in: (a) as–built (x-AB) state, (b) heat treatment (x-HT) state, (x = 0, 0.5, 1, 2 in wt. % of TiN).

microstructure and properties of SLM samples. The residual stress exhibited an upward trend for the AB sample with increasing TiN content. Specifically, the recorded values were 385 ± 80 MPa, 444 ± 90 MPa, 450 ± 50 MPa, and 557 ± 65 MPa for the 0–AB, 0.5–AB, 1–AB, and 2–AB samples.

Conversely, the RS values for the HT samples showed a slight reduction compared to the AB samples. Specifically, the 0–HT, 0.5–HT, 1–HT, and 2–HT samples exhibited RS values of 310 ± 50 MPa, 350 ± 60 MPa, 320 ± 40 MPa, and 405 ± 60 MPa, respectively. These findings confirm that the heat treatments could effectively alleviate the residual stress. The recrystallization and dissolution of cellular structures induced by the HT contributed to reducing RS [23]. Importantly, these

Table 1

The relative density measured by Archimedes method and phase composition determined by XRD of the SLM TiN–x samples (x = 0, 0.5, 1, 2 wt %) in both the as-built (AB) and heat treated (HT) states.

Sample	As-built (AB)				Heat treated (HT)			
	RD	α-phase	γ-phase	TiN	RD	α-phase	γ-phase	TiN
	wt. %	vol. %	vol. %	vol. %	wt. %	vol. %	vol. %	vol. %
TiN–0	99.51 ± 0.14	86.88 ± 0.43	13.12 ± 0.41	0.00 ± 0.00	99.60 ± 0.15	83.25 ± 0.56	16.75 ± 0.43	0.00 ± 0.00
TiN–0.5	99.45 ± 0.21	97.40 ± 0.19	2.49 ± 0.17	0.11 ± 0.04	99.53 ± 0.23	90.01 ± 0.36	9.89 ± 0.38	0.10 ± 0.02
TiN–1	99.41 ± 0.16	98.33 ± 0.52	1.66 ± 0.51	0.31 ± 0.03	99.45 ± 0.17	95.69 ± 0.17	4.01 ± 0.19	0.30 ± 0.03
TiN–2	99.22 ± 0.15	98.97 ± 0.38	0.15 ± 0.07	0.98 ± 0.03	99.24 ± 0.18	98.29 ± 0.15	0.61 ± 0.12	1.10 ± 0.04

results align with those reported in the previous research studies [24, 25].

3.3. Microstructure

Fig. 8 displays post-etching metallographic SEM images captured perpendicular to the building direction of both AB and HT samples. These images revealed cellular morphological structures. In Fig. 8a, the microstructure of the 0–AB sample exhibited a primary ring-like structure with lath martensite inside. The 0.5–AB, 1–AB, and 2–AB samples (Fig. 8a–d) exhibited primary cellular and lath martensite structures, along with a random distribution of TiN particles along grain boundaries and within grains.

Upon comparing the microstructures of AB samples with those of HT samples through SEM observation of the post-etching surface (as depicted in Fig. 8e and h), it was observed that the primary ring-like and lath structures exhibited similar shapes and sizes. The formation of cellular structures, induced by compositional fluctuation and constitutional supercooling during the SLM process, was evident. However, there was inherent unevenness in the distribution of cell sizes. This observation may be attributed to the phenomenon wherein the molten pool absorbed relatively minor laser energy but experienced rapid cooling rates [23]. Concurrently, the fluctuating direction of heat flow resulted in a disorderly pattern of structural growth, contributing to variations in the sizes of these cellular formations [26]. Further elucidation on the differences in the microstructure of AB and HT samples will be provided in Section 3.4.

Furthermore, the examination of grain boundaries revealed the predominant presence of TiN particles, indicating a high density of dislocations. This phenomenon was attributed to the elevated stress

generated by the rapid and repetitive heating and cooling cycles during the SLM process [1]. Given the relatively low TiN particle content in the matrix, XRD analysis failed to clearly detect TiN, as discussed in Section 3.1. Consequently, TEM and EDS compositional analysis were employed to elucidate the distribution of TiN particles in the AISI 420 matrix. As depicted in Fig. 9, nanoscale and microscale TiN particles were identified in Samples 1–AB and 2–AB. Moreover, the prevalence of TiN within the matrix exhibited a proportional increase with the TiN content. Fig. 9a indicated the remain of the micro TiN in the AISI 420 matrix. Fig. 9b illustrated that nearly all nanoscale TiN particles were localized within the grains, while microscale TiN particles were randomly dispersed throughout the matrix. This observation underscores the significant role played by TiN particles in influencing the SLM process. The consistent distribution of these TiN particles played a crucial role in achieving a uniform blend of powders during the powder mixing process.

A more detailed examination of the microstructures of the SLM TiN/ AISI 420 samples was conducted using TEM at higher magnification levels. Fig. 10a–c provides evidence of the distribution of TiN particles along grain boundaries for samples 0.5–AB, 1–AB, and 2–AB. To further magnify the details, Fig. 10d zooms in on the interface between TiN and martensite phase in Fig. 10c. The selected area electron diffraction (SAED) patterns in Fig. 10e and f confirmed the presence of both TiN and martensite phases in Fig. 10d. This analysis revealed a crucial observation: a significant atomic mismatch and localized strain at the interfaces between α-grains and TiN. This indicates that, from a crystallographic perspective, the TiN nanoparticles did not effectively act as nucleation sites to refine the grain structure, resulting in an enlarger in the α-microstructure achieved by adding TiN particles [12].

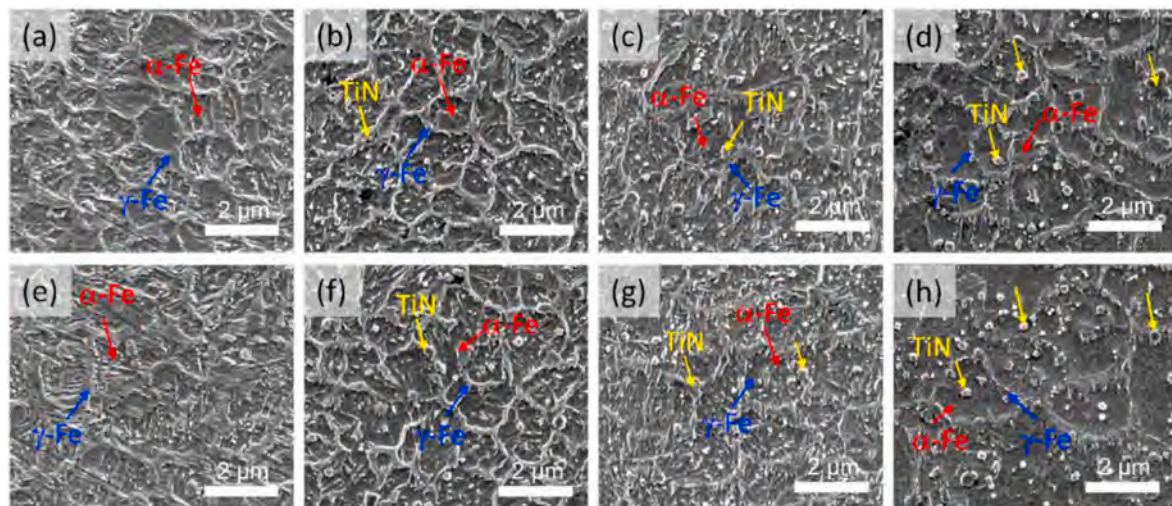For a more in-depth analysis of the SLM TiN/AISI 420 composite

Fig. 8. Displays SEM images of the etched surface of all x–TiN/AISI420 samples in both as-built states: (a) 0–AB, (b) 0.5–AB, (c) 1–AB, (d) 2–AB, and heat-treated states: (e) 0–HT, (f) 0.5–HT, (g) 1–HT, and (h) 2–HT. Yellow arrows highlight TiN particles at the boundaries within the AISI 420 matrix, while red and blue arrows indicate martensite and retained austenite phases, respectively. (For interpretation of the references to color in this figure legend, the reader is referred to the Web version of this article.)
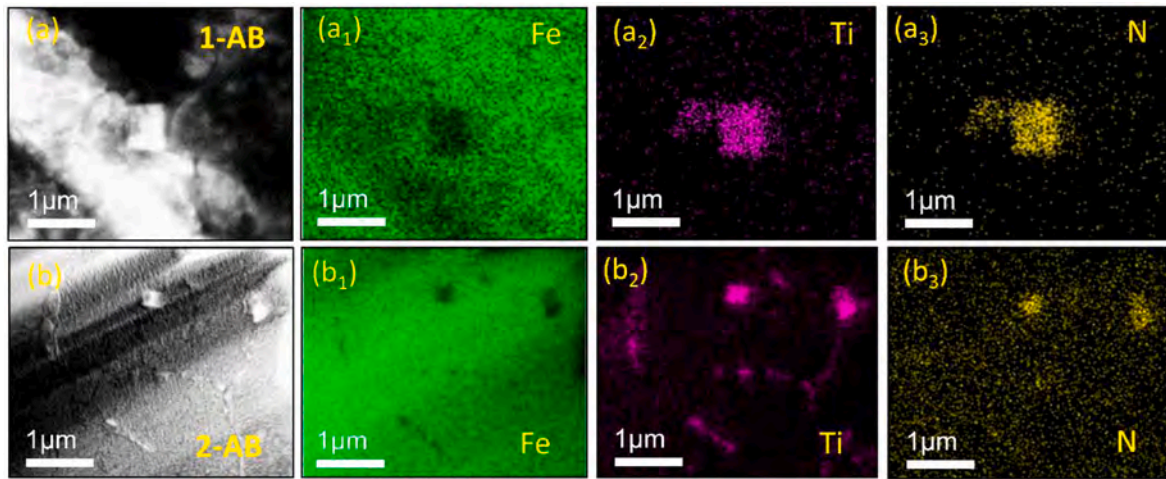
Fig. 9. Represents the TEM images and elemental profiles through EDS mapping of the SLM samples: (a) 1–AB, (b) 2–AB.
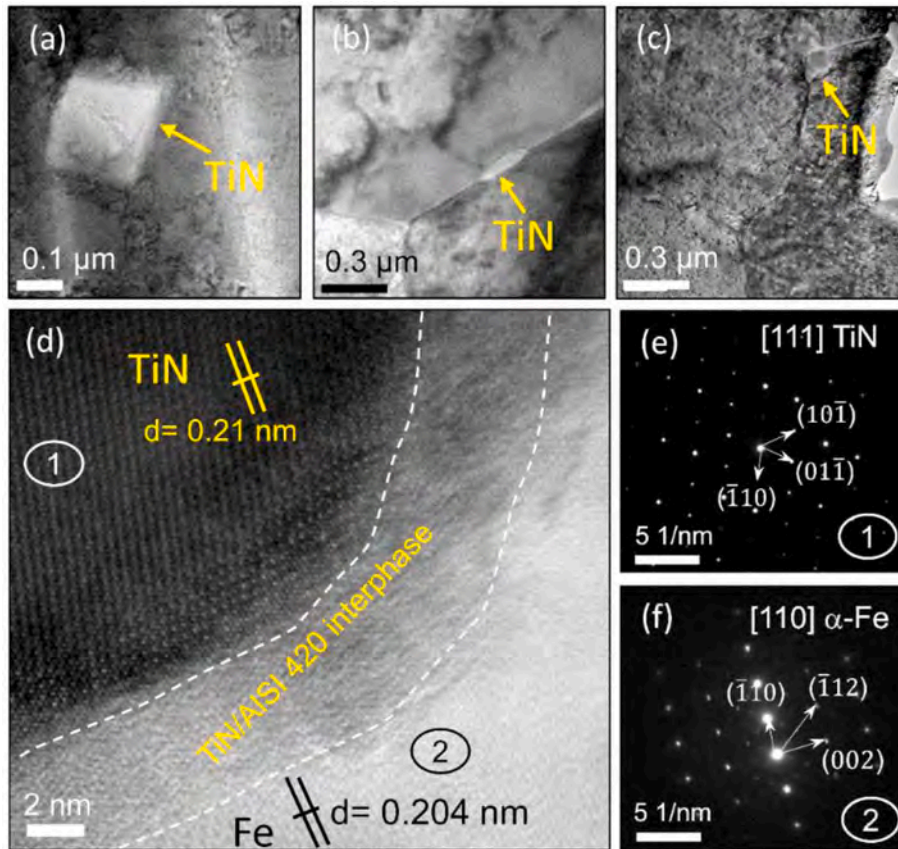

Fig. 10. Shows the cross-sectional TEM observations on TiN particles located on the grain boundary for the SLM TiN/AISI 420 samples in as-built (AB) state: (a) 0.5–AB, (b) 1–AB, (c) 2–AB; (d) illustrates the interphase of TiN and Fe matrix; Selected area electron diffraction (SAED) patterns of (e) and (f) correspond to patterns of regions 1 and 2 in (d).

sample structure, we performed TEM images for the TiN-1 samples. As shown in Fig. 11, the presence of sub-grains and dislocations nano-structure for both AB and HT samples suggested that it was highly relative to the material's performance and properties. In Fig. 11a and b, the small TiN particles were found at the grain boundary in both cases 1–AB and 1–HT, which supported the evidence presented in Fig. 11. In Fig. 11a, sub-grains were identified with a feature size of several tens of nanometers, and a high density of dislocations was observed. This could be attributed to the residual stress generated during the rapid cooling

process in the SLM process (Fig. 4b). Following the heat treatment procedure, minimal alteration was observed in the distribution and sub-grains, while a reduction in dislocation density was evident, as confirmed by TEM analysis depicted in Fig. 10b. Additionally, it was noted that dislocations along the grain boundary migrated and became undetectable following the heat treatment [27]. This reduction in dislocations after heat treatment is significant as it facilitates the alleviation of residual stress, a phenomenon elaborated upon in Section 3.2.
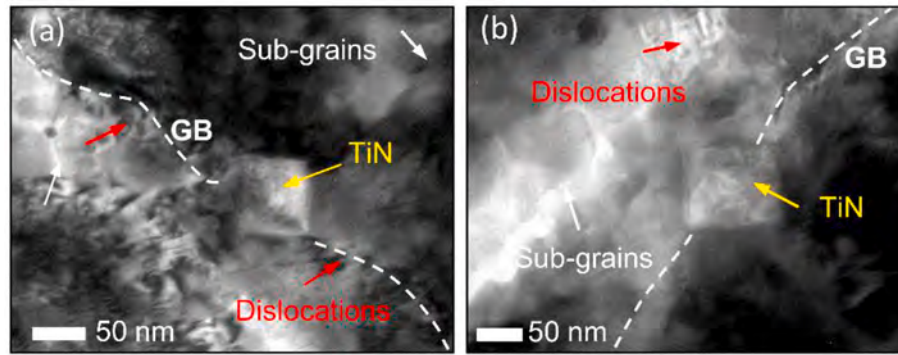
Fig. 11. Depicts the TEM images of (a) 1–AB and (b) 1–HT samples. Inserts include observations of TiN particles (yellow arrows), grain boundary (GB) denoted by white dash lines, sub-grains (white arrows), and dislocations (red arrows). (For interpretation of the references to color in this figure legend, the reader is referred to the Web version of this article.)

3.4. Crystallographic texture

The different crystallographic orientations on the transverse cross-sections of all AB and HT samples through EBSD inverse pole figures (IPFs) are shown in Fig. 12. The EBSD orientation maps provide insights into the grain features of all x-AB (Fig. 12a–d), and x-HT (Fig. 12e–h) samples. In these figures, orientations along directions <111>, <001>, and <101> are represented in blue, red, and green, respectively.

Initially, it is evident that both the AB and HT samples display an anisotropic structure, which arises from the rotational scanning strategy applied between successive layers in the SLM manufacturing process. Particularly noteworthy, the 1-AB and 1-HT samples (see Fig. 12c and g) exhibit a pronounced orientation along the <111> direction. The IPF maps of these samples (depicted in Fig. 13c and g) reveal a peak texture index of 3. This observation confirms that a preferred <111> texture is established in a longitudinal cross-section aligned with the building direction. Conversely, the remaining samples (0–AB, 0.5–AB, 2–AB, 0–HT, 0.5–HT, and 2–HT) do not manifest any distinct preferred grain orientation. Instead, a random distribution of grains is discernible in the EBSD maps, as evidenced by their low intensity, below 1.6 (as illustrated in Figs. 12 and 13).

In addition, based on the EBSD results, the microstructure of AB and HT samples was also analyzed. As shown in Fig. 12a–d and 12e-g, the microstructure features of 0–AB, 0.5–AB, 1–AB, 0–HT, 0.5–HT, and 1–HT samples exhibit discernible blocks and packets, characteristic of the lath structures as elucidated by Morito et al. [27] and Kithara et al. [28]. This structure aligns with the one defined in Fig. 8. However, the grain structure of the 2–AB, 2–HT samples primarily comprises coarse quasi-equiaxed grains (Fig. 12e and h). This observation suggests a notable influence of high-content TiN particles in augmenting the grains' size and structure.

The effect of TiN content and heat treatment on the grain size and phase composition of the AB TiN/AISI 420 samples was further studied. Fig. 14 depicts the grain distribution and phase composition of the AB and HT samples. The grain size and EBSD phase composition of the AB samples could be quantified and observed from Fig. 14a$_1$ – 14d$_1$. The results indicated that the grain size increased with an elevated TiN particle content. Precisely, the grain sizes for 0–AB, 0.5–AB, 1–AB, and 2–AB were measured at 1.11 μm, 1.19 μm, 1.56 μm, and 2.33 μm, respectively. The existence of TiN particles influenced the crystallographic orientation, phase composition, and grain size of the SLM samples, thereby substantiating their roles in shaping the material's microstructural attributes and mechanical properties [8]. Moreover, the phase mappings of AB samples are depicted in Fig. 14a$_2$ – 14d$_2$ and detailed in Table 2. The martensite phase (indicated by the red area) predominated, with volume relative percentages of 89.01 ± 0.11 vol %,
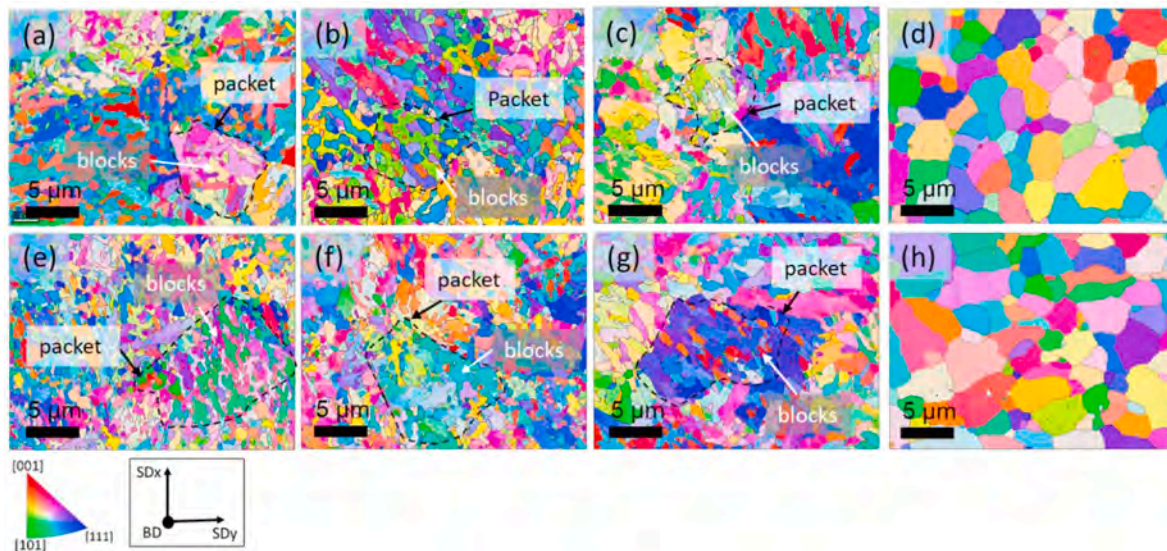
Fig. 12. Indicates EBSD orientation maps from the top view of the as-built (AB) samples, (a)–(d), including (a) 0–AB, (b) 0.5–AB, (c) 1–AB, (d) 2–AB; as well as the heat treatment samples (HT), (e)–(h), denoted as: (e) 0–HT, (f) 0.5–HT, (g) 1–HT, (h) 2–HT; The inversed pole figure (IPF) for EBSD orientation maps in depicted at the bottom left corner. The building direction (BD) and laser scanning directions SD$_x$ and SD$_y$ are also illustrated at the bottom.

Fig. 13. Shows the inversed pole figures (IPFs) intensity for EBSD orientation maps of all AB and HT samples.
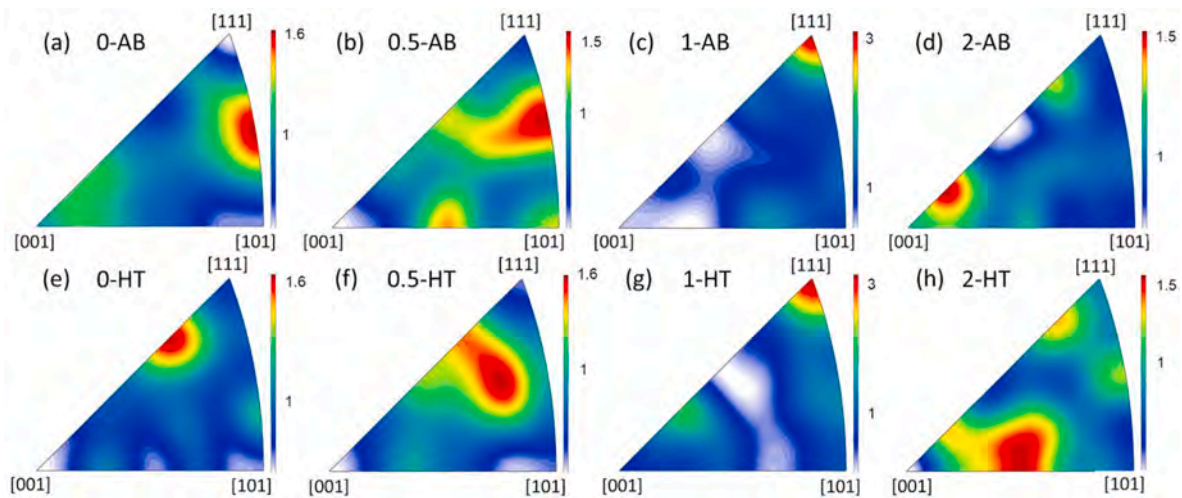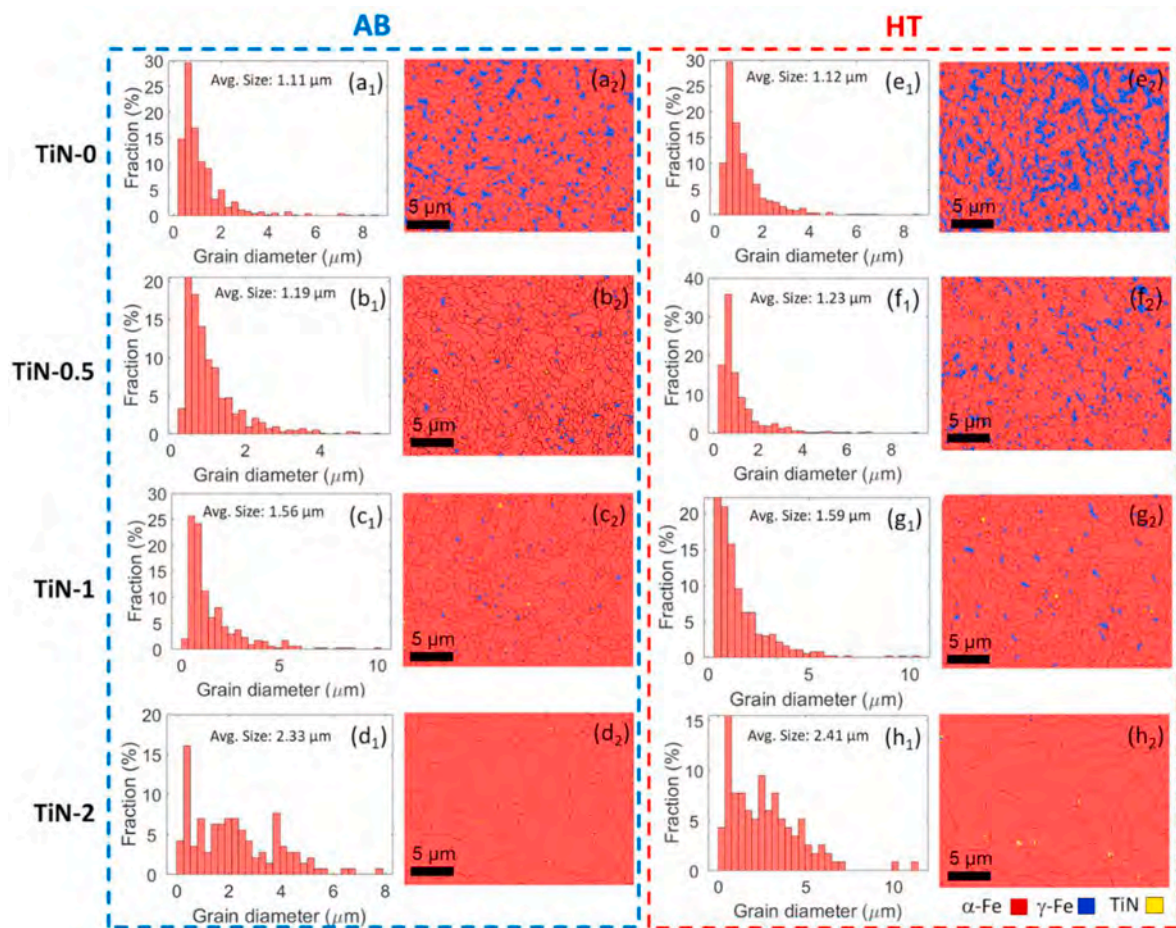

Fig. 14. Illustrates grain size distribution maps, denoted as (a₁) – (h₁), along with corresponding phase compositions, denoted as (a₂) – (h₂), of the SLM TiN/AISI 420 samples. Panels (a)–(d) represent the as-built states: (a) 0–AB, (b) 0.5–AB, (c) 1–AB, and (d) 2–AB; whereas panels (e)–(h) pertain to the heat treatment states: (e) 0–HT, (f) 0.5–HT, (g) 1–HT, and (h) 2–HT. In panels (a₂) – (h₂), the phases' compositions are depicted, with the martensite phase indicated by the red region, retained austenite represented by the blue region, and TiN denoted by the yellow region. (For interpretation of the references to color in this figure legend, the reader is referred to the Web version of this article.)

97.03 ± 0.14 vol %, 97.94 ± 0.03 vol %, and 98.12 ± 0.14 vol % for 0–AB, 0.5–AB, 1–AB, and 2–AB, respectively. Interestingly, the retained austenite phase (depicted in the blue area) diminished with increased TiN content, exhibiting 11.00 ± 0.14 vol %, 2.70 ± 0.07 vol %, 1.25 ±

0.10 vol %, and 0.37 ± 0.11 vol % values for 0–AB, 0.5–AB, 1–AB, and 2–AB, respectively. The TiN phase composition, represented by the yellow color, increased with higher TiN content, with proportions of 0 vol %, 0.30 ± 0.04 vol %, 0.81 ± 0.11 vol %, and 1.50 ± 0.02 vol %,

Table 2
The phase composition of SLM TiN-x samples (x = 0, 0.5, 1, 2 wt %) detected by EBSD.

Sample	As-built (AB)			Heat treated (HT)		
	α-phase	γ-phase	TiN	α-phase	γ-phase	TiN
	vol. %	vol. %	vol. %	vol. %	vol. %	vol. %
TiN–0	89.01 ± 0.11	11.0 ± 0.14	0.00 ± 0.00	74.15 ± 0.15	25.85 ± 0.04	0.00 ± 0.00
TiN–0.5	97.03 ± 0.14	2.7 ± 0.07	0.30 ± 0.04	93.11 ± 0.24	6.57 ± 0.10	0.32 ± 0.03
TiN–1	97.94 ± 0.03	1.25 ± 0.10	0.81 ± 0.11	96.03 ± 0.17	3.12 ± 0.11	0.85 ± 0.06
TiN–2	98.12 ± 0.14	0.37 ± 0.11	1.50 ± 0.02	97.05 ± 0.2	1.51 ± 0.08	1.44 ± 0.04

Table 3
Mechanical properties of the SLM TiN-x samples (x = 0, 0.5, 1, 2 wt %) in both AB and HT states.

Sample	Yield strength	Tensile strength	Elongation	Hardness	Toughness
	MPa	MPa	%	HV	J/m^3
0–AB	983 ± 40	1203 ± 31	2.1 ± 0.1	678 ± 16	21.3 ± 0.6
0.5–AB	1290 ± 25	1520 ± 15	3.0 ± 0.1	725 ± 15	37.0 ± 1.5
1–AB	1359 ± 35	1618 ± 15	3.2 ± 0.1	745 ± 12	42.2 ± 0.4
2–AB	997 ± 35	1220 ± 45	3.5 ± 0.3	610 ± 20	36.2 ± 0.7
0–HT	1118 ± 25	1601 ± 40	4.8 ± 0.3	574 ± 14	60.6 ± 2.6
0.5–HT	1350 ± 17	1725 ± 36	6.1 ± 0.2	650 ± 20	88.0 ± 1.3
1–HT	1440 ± 27	1860 ± 36	7.3 ± 0.2	685 ± 15	118.0 ± 1.3
2–HT	1016 ± 8	1288 ± 28	5.1 ± 0.1	540 ± 10	56.9 ± 1.3

respectively. This characterization of phase composition aligned well with the XRD pattern presented in Section 3.1.

Furthermore, Fig. 14e–h enable the quantification and observation of the grain size and EBSD phase composition of the HT TiN/AISI 420 samples. In comparison to their AB counterparts, the HT samples exhibited a slight increase in grain size, measuring 1.12 μm, 1.23 μm, 1.59 μm, and 2.41 μm for 0–HT, 0.5–HT, 1–HT, and 2–HT samples, respectively (Fig. 14e$_1$ – 14h$_1$). Additionally, the phase mapping of HT samples, as presented in Fig. 14e$_2$ – 14h$_2$, revealed discernible compositional alterations compared to the microstructures of the AB samples. All HT samples manifested a notable increase in RA content compared to their AB counterparts, which were 25.85 ± 0.04 vol %, 6.57 ± 0.1 vol %, 3.12 ± 0.11 vol %, and 1.51 ± 0.08 vol % for 0–HT, 0.5–HT, 1–HT, and 2–HT samples, respectively. The heightened content of retained austenite in the structure can be attributed to the martensite-austenite transformation during the heat treatment [15].

3.5. Mechanical properties

For a comprehensive evaluation of the influence of TiN addition and subsequent heat treatment on mechanical properties, such as: Vickers hardness tests and uniaxial tensile tests, were systematically conducted on both AB and HT samples for TiN–0, TiN–0.5, TiN–1, and TiN–2. Fig. 15 and Table 3 summarize the condensed results succinctly. As discerned from Fig. 15a, the Vickers hardness of 1–AB was highest with 745 ± 12 H V, notably surpassing the value of 0.5–AB and 0–AB are 725 ± 15 H V and 678 ± 16 H V, respectively. Conversely, the hardness values of 2–AB, quantified at 610 ± 20 H V, registered considerable reductions of approximately 10 % compared to 0–AB. The primary factors contributing to the observed hardness disparities stemmed from the variations in grain size and TiN distribution within the AB samples. Intriguingly, the grain size of 1–AB approximated 1.56 μm, slightly higher than that of 0–AB (1.11 μm). However, the heightened hardness observed in 1–AB was attributed to the reinforcing effect of TiN particles, which hindered dislocations along grain boundaries. In contrast,

the expanded grain dimensions witnessed in 2–AB samples, surpassing 2 μm, resulted from an augmented prevalence of TiN particles within the microstructure. This expansion in grain size emerged as the primary determinant for the observed reduction in hardness, as corroborated by the insights garnered from EBSD analyses (Fig. 14a$_1$ – d$_1$).

Furthermore, after subjecting the samples to the heat treatment protocol, a noticeable decrease in hardness was observed in the 0–HT, 0.5–HT, and 1–HT samples, resulting in values of 574 ± 14 H V, 650 ± 20 H V and 685 ± 15 H V, respectively. These values represented a reduction of 13.7 %, 10.3 %, and 8.1 % compared to the hardness of the 0–AB, 0.5–AB, and 1–AB samples, respectively. Investigation into the outcomes of EBSD provided insights into the mechanisms underlying this decline in hardness in the HT samples, primarily attributed to an increase in grain size and an augmented presence of γ–Fe following the tempering process (Fig. 14e–g). Conversely, the hardness measurements of the 2–HT samples exhibited only minor deviations from their corresponding 2–AB states. This consistency in hardness could be attributed to the stabilization of grain size and phase composition maintained throughout the heat treatment procedure for these particular specimens (Fig. 14h).

The stress-strain curves corresponding to the AB and HT samples are graphically represented in Fig. 14b, and Table 3. In the AB cases, the tensile strength of the 0–AB sample was measured at 1203 ± 31 MPa. Notably, when the TiN content was incremented to 0.5 wt % and 1.0 wt %, the tensile strength increased significantly to 1520 ± 15 MPa and 1618 ± 15 MPa, signifying a substantial 26.4 % and 34.5 % augmentation relative to the 0-AB sample, respectively. With further escalation of the TiN content to 2 wt%, (2–AB), the tensile strength diminished to 1220 ± 45 MPa. This reduction could be attributed to two main factors: firstly, the increase in structural defects due to the decrease in relative density; and secondly, the agglomeration of TiN particles diminishing the wetting ability between TiN and AISI 420, compromising the strengthening mechanism and ultimately resulting in a reduction in strength. Interestingly, the elongation properties of 0.5–AB, 1–AB, and
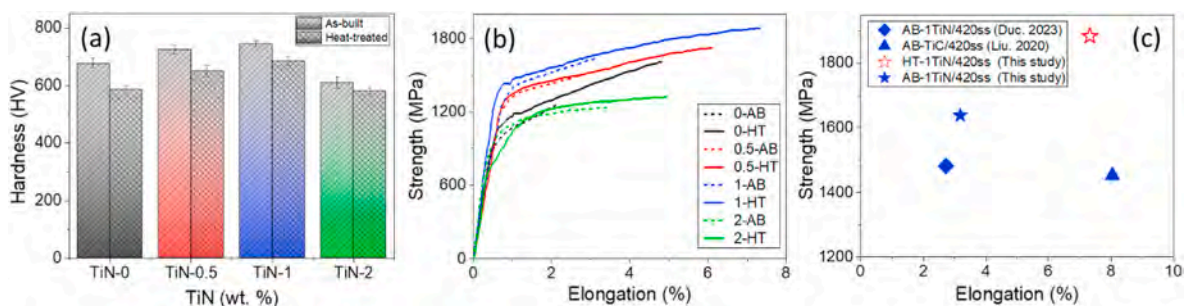

Fig. 15. Illustrates the diagram of (a) the hardness, (b) tensile stress-strain curves of the SLM TiN/AISI 420 samples in AB and HT states, and (c) a comparison of the tensile strength and elongation obtained in this study with other researches (blue points for AB SLM and red point for HT samples). (For interpretation of the references to color in this figure legend, the reader is referred to the Web version of this article.)

2–AB samples achieved approximately 3.0 ± 0.1 %, 3.2 ± 0.1 %, and 3.5 ± 0.3 %, respectively, surpassing that of the TiN–0 counterpart of 2.1 ± 0.1 %. Therefore, the modulus of toughness for the AB samples was derived from the stress-strain curves. Consequently, the incorporation of the TiN nanoparticles yielded a notable enhancement in the modulus of toughness. Specifically, values of 37.0 ± 1.5 J/m^3, 42.2 ± 0.4 J/m^3, and 36.2 ± 0.7 J/m^3 were achieved for 0.5–AB, 1–AB, and 2–AB, respectively. These values represented enhancements of 76.2 %, 98.1 %, and 70 %, respectively, compared to the modulus of toughness exhibited by the unmodified 0–AB of 21.3 ± 0.6 J/m^3.

Wherein after the tempering process, a discernible trend was observed; the tensile strength and elongation of all tempered specimens exhibit noteworthy enhancement compared to the AB counterparts (Fig. 15b). The tensile strength of 0–HT, 0.5–HT, 1–HT, and 2–HT were 1601 ± 40, 1725 ± 26 MPa, 1860 ± 36 MPa, and 1288 ± 28 MPa, which demonstrated an increase of 33.8 %, 13.5 %, 14.5 %, and 5.6 % compared to the corresponding AB samples, respectively. Similarly, the elongation values depicted substantial enhancements, with the value of 0–HT, 0.5–HT, 1–HT, and 2–HT being 4.8 ± 0.3 %, 6.1 ± 0.2 %, 7.3 ± 0.2 %, and 5.1 ± 0.1 %, showing an increase of 128.6 %, 103 %, 128 % and 45.7 %, compared to the counterpart. The notable elevation observed in tensile strength and elongation after the tempering process contributed to a commendable enhancement in the HT samples' modulus of ultimate toughness. The peak toughness exhibited by 1–HT was particularly noteworthy, attaining a value of 118 ± 1.3 J/m^3. Sequentially, the ranking of toughness values follows with 60.6 ± 2.6 J/m^3, 88.0 ± 1.3 J/m^3, and 56.9 ± 1.3 J/m^3 for 0–HT, 0.5–HT, and 2–HT, respectively.

This study investigated the tensile strength and elongation of the 1–AB sample and compared them with the SLM 1%TiN/AISI 420 sample from our prior research. As shown in Fig. 15c, the 1–AB sample demonstrated superior tensile strength and elongation properties compared to the preceding sample. Specifically, the 1–AB sample had a tensile strength of 1618 MPa and an elongation of 3.2 %, while the prior sample had a tensile strength of 1270 MPa and an elongation of 2.7 % [7]. Furthermore, we conducted a heat treatment process on the samples to investigate the effect of tempering on their properties. After the tempering process, we found that the tensile strength and elongation of the 1–HT sample exceeded those reported for the existing TiN/AISI 420 sample. In fact, the 1–HT sample had a tensile strength of 1860 MPa, which was even higher than the SLM TiC/AISI 420 sample reported by Liu et al. [29] (with a tensile strength of 1482 MPa). However, it is essential to note that the elongation of the 1–HT sample was slightly lower than that of the SLM TiC/AISI 420 sample. This implies that while the 1–HT sample exhibited superior tensile strength properties, the SLM TiC/AISI 420 sample demonstrated better elongation properties. Our findings suggest that the 1–AB and 1–HT samples have superior tensile strength properties compared to prior research and existing TiN/AISI 420 and TiC/AISI 420 samples, respectively. However, further research is needed to investigate the impact of elongation properties on the performance of these samples in specific applications.

3.6. Fracture morphologies

The fractographies by tensile testing of the SLM AB and HT TiN/AISI 420 samples were illustrated in Fig. 16. These help to gain a deeper insight into the underlying fracture mechanisms. In Fig. 16a–d, the fracture surfaces of 0–AB, 1–AB, 1–AB, and 2–AB samples manifested a distinctive brittle failure mode characterized by a multitude of discernible cleavage facets. Notably, the fracture surface of 0–AB revealed the presence of inclusions, yielding the lowest elongation. Upon the introduction of TiN particles into the samples, particularly with a high content of TiN (2 wt%), the aggregation of these particles and their subsequent contribution to the fracture process became apparent, as depicted in Fig. 16d. The emergence of dimples on the fracture surfaces, as depicted in Fig. 16e–h was a pivotal factor contributing to the increased elongation observed in all HT samples. These dimples, marked by a scarcity of cracks, played a central role in enhancing the elongation of 0.5–HT, 1–HT. Conversely, inclusions (exhibited in 0–HT) and fractures within the TiN particles (shown in 2–HT) constituted the primary factors leading to diminished tensile strength and elongation.

3.7. Corrosion resistance

The effectiveness of the *CR* of the SLM x–TiN/AISI 420 (x = 0, 0.5, 1 and 2 wt%) samples was evaluated through immersion in a 6 wt% ferric chloride solution at 50 °C for 48 h (in Section 2.3). The results are depicted in Fig. 4c, and elaborated in Table 4. Corrosion rate (CR_t) measurements were used to gauge the speed of corrosion, a lower CR_t values indicating higher *CR* ability [30]. Fig. 15 illustrates a reduction in CR_t with increased TiN content within the SLM samples. Specifically, for the 0–AB, 0.5–AB, 1–AB, and 2–AB samples, the CR_t values were recorded at 120.1 ± 2.6 mm/year, 114.5 ± 2.7 mm/year, 112.8 ± 2.6 mm/year, and 105.6 ± 2.5 mm/year, respectively (see Table 4). This pattern was similarly noticeable in the HT samples, where a higher TiN
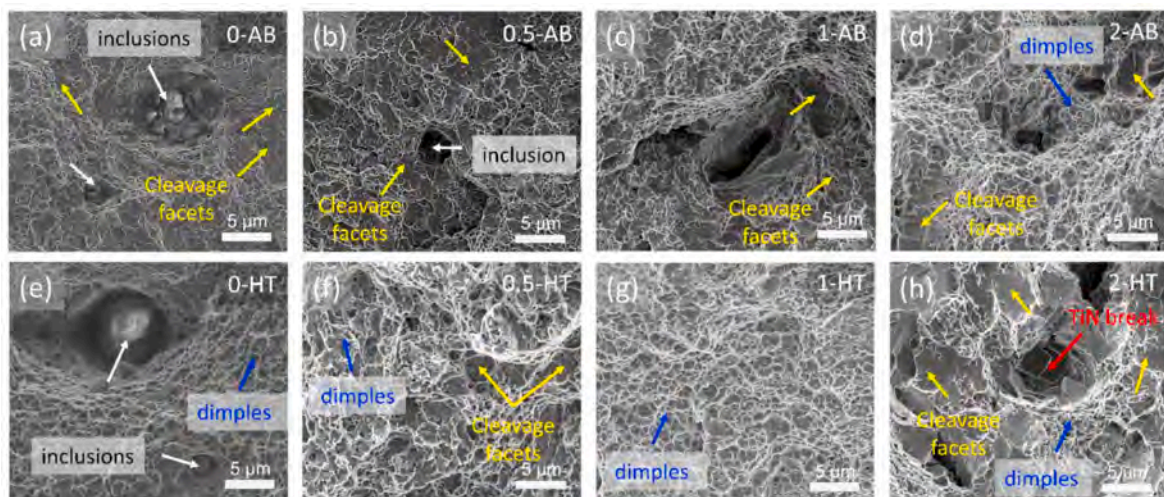

Fig. 16. Represents the fracture morphologies of the TiN/AISI 420 samples in as-built (AB) and post-heat treatment (HT) state, whereas: (a) 0–AB, (b) 0.5–AB, (c) 1–AB, (d) 2–AB; (e) 0–HT, (f) 0.5–HT, (g) 1–HT, and (h) 2–HT.

Table 4
The corrosion properties of the SLM TiN-x samples (x = 0, 0.5, 1, 2 wt %) in 6 wt % ferric chloride in both cases of AB and HT.

Sample	Bulk density	Corrosive area, (A)	Time, (T)	Weight loss, (W)	Corrosion rate, (CR_t)
	g/cm^3	cm^2	hour	mg	mm/year
0–AB	7.702 ± 0.011	1.0	48	506 ± 11	120.1 ± 2.6
0.5–AB	7.687 ± 0.016	1.0	48	482 ± 12	114.5 ± 2.7
1–AB	7.674 ± 0.012	1.0	48	474 ± 10	112.8 ± 2.6
2–AB	7.631 ± 0.011	1.0	48	442 ± 11	105.6 ± 2.5
0–HT	7.709 ± 0.012	1.0	48	503 ± 11	119.3 ± 2.6
0.5–HT	7.694 ± 0.018	1.0	48	480 ± 10	114.0 ± 2.5
1–HT	7.678 ± 0.013	1.0	48	462 ± 12	110.0 ± 2.8
2–HT	7.632 ± 0.014	1.0	48	437 ± 12	104.7 ± 2.7

content corresponded to an enhanced ability to resist corrosion. Furthermore, all the CR_t values of the HT samples were lower than those of their AB counterparts. Specifically, the CR_t value for 0–HT was 119.3 ± 2.6 mm/year, 0.5–HT was 114.0 ± 2.5 mm/year, 1–HT was 110.0 ± 2.8 mm/year, and 2–HT was 104.7 ± 2.7 mm/year. It could be concluded that the SLM samples exhibited an improved ability to resist corrosion after the HT processing. The transformation of the martensite-austenite phase during the HT procedure increased the austenite phase, consequently enhancing the CR of the HT sample.

4. Discussion

4.1. TiN content and distribution in SLM TiN/AISI 420 composite

Upon examining the microstructure, mechanical properties, and corrosion behavior of SLM TiN/AISI 420 samples, it became evident that the quantity and arrangement of TiN particles within the AISI 420 matrix played a pivotal role in shaping these characteristics. Therefore, obtaining a comprehensive understanding of how TiN dispersed within the AISI 420 matrix was imperative for accurately interpreting the observed outcomes. Within the AISI 420 matrix, TiN particles were identified as impurities during the molten stainless steel phase in the SLM process [8], exerting an influence on laser absorption [16]. The XRD results revealed that no new phases from TiN were generated in the resulting matrix, indicating that the bonding of TiN persisted during the SLM process due to its high melting point (2930 °C), surpassing that of AISI 420 (1470–1510 °C). This persistence is further corroborated by nanoscale observations, as illustrated in Fig. 10.

Moreover, it is essential to highlight that the laser absorption capacity of TiN/AISI 420 diminishes with an increase in TiN content within the AISI 420 matrix. This emphasizes the intricate relationship between the quantity of TiN and the efficiency of laser absorption in this composite. Consequently, a higher TiN content reduces the ability of the powder mixture to absorb laser energy. This reduction is attributed to the absorption coefficient of TiN powder for the 1060 nm–wavelength laser, which is 0.32 [17], lower than steel powder at 0.6 [31]. This alteration significantly influences the onset, configuration, and duration of the melting pool during the SLM process.

In the SLM process, a laser beam with high energy density was utilized to melt a powder mixture, as depicted in Fig. 17a. The laser scanning method in SLM caused the region where the focused laser beam interacted with the powder to be preheated before laser irradiation, owing to heat conduction. Consequently, within the area of laser-powder interaction, a plasma phase could be locally generated along the laser path. The combination of high temperatures, high pressures, and transition mismatches between liquid and solid phases might expel molten materials and powders. Additionally, the surface tension of the molten surface contributes to the formation of the surface finish. Fig. 17a also illustrates the presence of the melt pool and solidification zone in the process.

In Figs. 8–12, the outcomes delineated the distribution of TiN in the microstructure of the TiN/AISI420 sample. At lower TiN content, TiN was observed to be distributed along grain boundaries. However, with higher content, specifically up to 2 wt%, the presence and clustering of TiN within the AISI 420 matrix became noticeable both at grain boundaries and within the grains, as depicted in Fig. 8d and h. Several factors influence the dispersion of TiN into the AISI 420 matrix, including (i) solidification rate [32,33], (ii) kinetics of the molten pool [33], (iii) quantity of TiN [9,34], and (iv) thermal expansion mismatch between TiN and AISI 420 [16].

First, during laser-induced melting, TiN particles' motion in the molten pool was lower than the motion speed of the solidification front [32]. This resulted in TiN particles being captured by the solidification front and subsequently distributed within the formed grains. Secondly, concerning the kinetics of the molten pool, the primary force responsible for rearranging and dispersing particles was Marangoni convection, generated by the surface capillary force induced owing to the high-temperature gradient along the free surface [33]. An equation expresses Marangoni convection, M_a, in the molten pool, $M_a = \Delta\sigma.L/(\mu_d.\nu_k)$, where $\Delta\sigma$ is the surface tension for the Marangoni flow, L is the length of a free surface, μ_d is dynamic viscosity, and ν_k is the kinetic velocity. Since μ_d is inversely proportional to the temperature in the molten pool (T_m), and T_m is proportional to the amount of laser absorption energy (E_b), but E_b is inversely proportional to TiN content; consequently, the M_a convection is inversely proportional to TiN content. This suggested that an increase in TiN wt. % resulted in a decrease in M_a. The reduction in M_a significantly influenced the microstructure of solidified TiN/AISI 420 composites. The slower movement of the molten pool allowed TiN to agglomerate at a higher frequency, leading to its distribution within the matrix during the solidification process. In addition, TiN rearrangement was influenced by van der Waals (VDW) interactions. The strength of VDW forces is inversely proportional to the distance between two nanoparticles within the molten metal. When the nanoparticle size was smaller than the atomic layers of the molten metal, VDW forces contributed more to the interfacial energy of the system than interfacial chemical bonding [9,34].

Therefore, with lower TiN content in the matrix, increased laser energy resulted in higher Marangoni convection, reduced van der Waals forces, and even dispersion of TiN within AISI 420. This phenomenon explained the formation of smaller grain sizes, as observed in Fig. 17b. Conversely, as TiN content increased, the impact of laser energy diminished, primarily reducing Marangoni convection and promoting TiN agglomeration. TiN particles then acted as barriers, hindering the formation of smaller grains during the solidification of the TiN/AISI 420 molten pool, as depicted in Fig. 17c. In addition to this, thermal expansion mismatch was another factor contributing to larger grain sizes with increasing the TiN content. The significant difference in thermal expansion between TiN and AISI 420 could induce internal stresses during heating and cooling cycles [16]. These stresses, in turn, led to the movement and growth of grain boundaries within the metal matrix, ultimately resulting in larger grain sizes.

4.2. Effect of heat treatment on mechanical properties

In this study, the heat treatment process involving annealing at 400 °C for 1 h and tempering at 200 °C for 2 h not only had an impact on residual stress but also influenced phase transformation, resulting in changes in the hardness and tensile properties of the resulting SLM TiN/AISI 420 samples. This section focuses on analyzing its effects on the sample exhibiting the best mechanical properties, which corresponds to
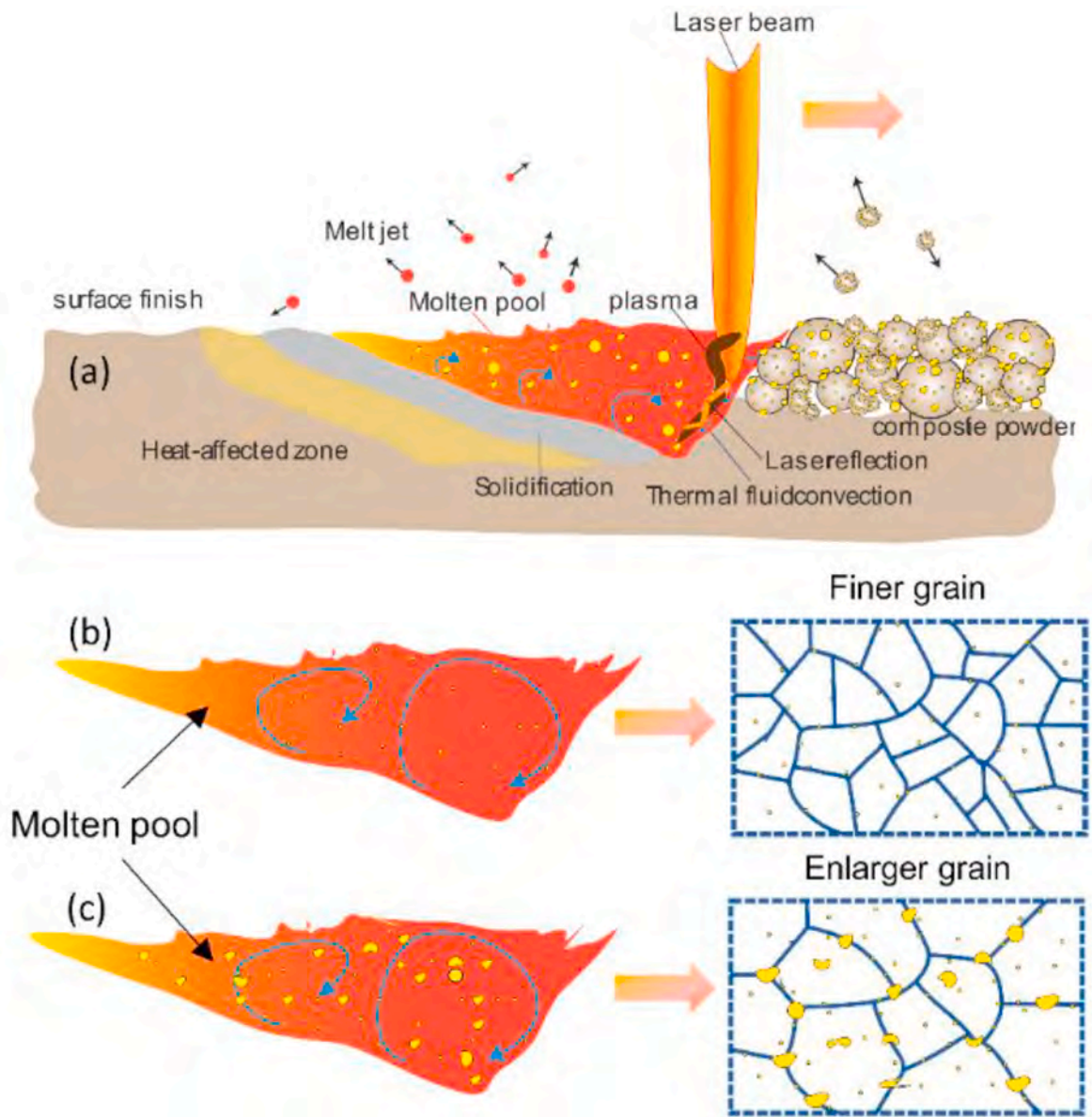
Fig. 17. Illustrates (a) the mechanism of selective laser melting; and (b), (c) the schematics for formatting the microstructure TiN/AISI 420 through SLM process, (the unmelted TiN is located both along grain boundaries and inside the grains, depending on the content of TiN in the melting pool).

the TiN–1 samples. The hardness of the 1–AB sample decreased after the heat treatment. The presence of a high content of martensitic phase and tiny grain size (around 1.5 μm) in the 1–AB samples (Fig. 14c$_1$ and 14c$_2$), coupled with elevated surface residual stress, contributed to a notable increase in hardness, reaching 745 ± 12 H V. However, after the heat treatment, recrystallization occurred [25], resulting in slight adjustments to grain size and phase configuration. There was also an increase in retained austenite, rising from 1.2 % to 3.2 % (as observed in EBSD results, Fig. 14c$_2$ and 14g$_2$). Additionally, the residual stress decreased from 450 MPa to 320 MPa, which explained the reduction in surface hardness.

Furthermore, the heat treatment applied to the SLM TiN/AISI 420 sample (Fig. 15b) yielded notable enhancements in both tensile strength and elongation for several discernible reasons: i) a decrease in dislocation density facilitated easier migration of dislocations during tensile testing. The reduction in partially melted particles and pores, known to initiate crack formation, contributed to the increased ductility observed post-heat treatment; ii) the reduction in residual stress (Fig. 4b) and restructuring of crystalline phases facilitated moving the grain

orientation from <111> to <101> following tensile testing (Fig. 13g and 18d). These transformations significantly bolstered the tensile strength, as documented in the literature [35]; iii) Grain refinement (0.92 μm) (Fig. 18b) was an effective way for simultaneously improving strength and ductility [36–38], and iv) transformation-induced plasticity (TRIP) effects further strengthened the material, as evidenced by the decrease in retained austenite content from 3.2 % to 2.1 % (depicted in Fig. 14f$_2$ and Fig. 18c). This reduction indicates the transformation of austenite to martensite during loading and deformation, a phenomenon well-documented in the literature [15,38].

4.3. Effects of TiN existence and post-heat treatment on corrosion resistance

The presence of the Cr element in AISI 420 led to the formation of a passive Cr$_2$O$_3$ film on the surface of the SLM sample [39]. As illustrated in Fig. 4c, the *CR$_t$* of SLM AB and HT samples decreased with the rise of the TiN content. Hence, exhibiting TiN particles emerges as a pivotal factor in altering corrosion kinetics and impacting the corrosion
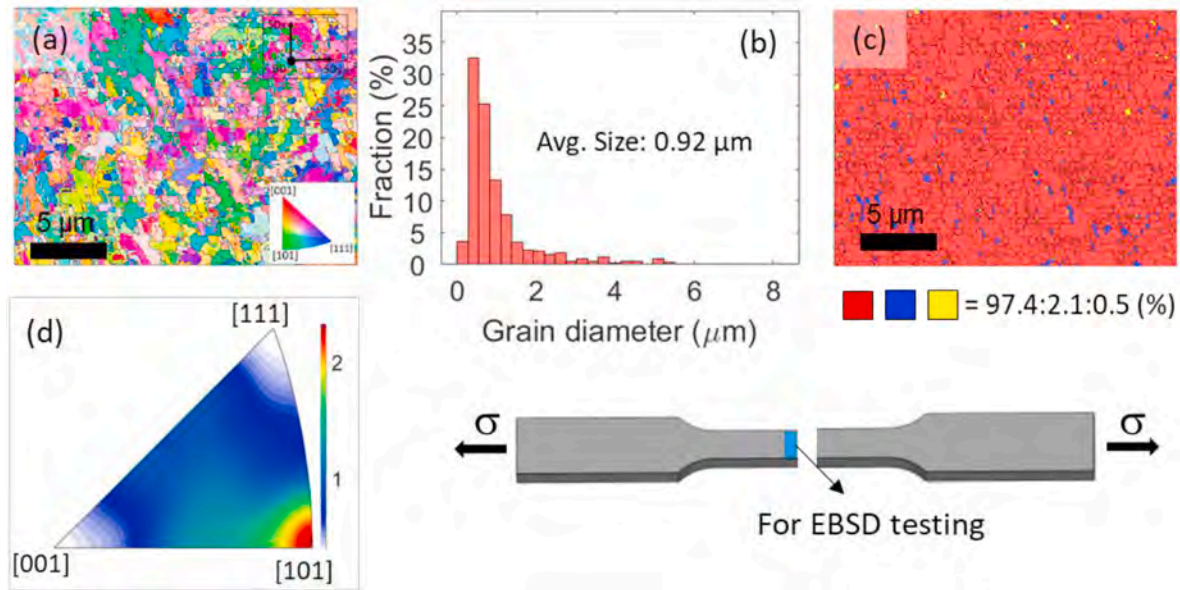
Fig. 18. Shows (a) the orientation, (b) grain size and (c) phase map (d) IPF for the 1–HT sample after tensile deformation.

behavior of the resultant SLM TiN/AISI 420 composites.

The progression of surface corrosion on the SLM AISI 420 sample in an oxidation environment could be outlined as follows: initially, tiny indentations emerge on the surface, which subsequently expand in size due to the impact of the corrosive surroundings, ultimately forming corrosion pits [40]. The initiation of this process often took place at active corrosion sites, which then evolved into micro-pitting, attributable to the impact of corrosive anions (Fe^{3+}) and the localized breakdown of the passive film layer. Then, the micro-pitting continued to expand, contingent upon the specific localized corrosive conditions, the re-passivation process, and the interplay between the micro-pits, as illustrated in the schematic Fig. 19a₁, and further corroborated by optical images in Fig. 19a₂.

To provide further evidence of the mechanisms of corrosion and the effectiveness of corrosion prevention, we present the Fe 2p, Cr 2p and Ti 2p XPS spectrum in Fig. 20 to confirm the formation of corrosive and anti-corrosive compounds. Specifically, in Fig. 20a, the Fe 2p energy level was composed of two characteristic peaks of two core level binding energies of Fe $2p_{1/2}$ and $2p_{3/2}$, at 724.6 eV and 710.9 eV, respectively. At

Fe $2p_{1/2}$ peak for the 0-AB sample reveals a secondary peak for Fe_2O_3 and Fe–Cr–O, with binding energies of 724.0 eV and 725.0 eV, respectively, consistent with the literature [41,42]. Moreover, at binding energies of 710.6 eV and 711.0 eV for Fe $2p_{3/2}$, Fe–Cr–O and Fe oxide were detected, aligning with research [43,44]. These findings confirm the reaction of Fe leading to the formation of Fe_2O_3, Fe^{2+}, and Fe–Cr–O on the corrosion surface. Additionally, comparison with data from the NIST database, the Cr 2p contrains 2 main peaks Cr $2p_{1/2}$ and Cr $2p_{3/2}$ at 586.6 eV and 576.6 eV, respective (as seen in Fig. 20b). The Cr 2p XPS signal also revealed the presence of Cr_2O_3 and CrO_2 in both Cr $2p_{1/2}$ and Cr $2p_{3/2}$ peaks in the 0–AB samples, suggesting the formation of a protective Cr_2O_3 oxide layer on the SLM AISI 420 sample's surface. Notably, the Ti 2p element was not detected in the 0-AB sample, correlating with the absence of TiN in the AISI 420 matrix (Fig. 20c).

Incorporating TiN into the SLM AISI 420 matrix for the TiN/AISI 420 samples significantly alters the corrosion mechanism (Fig. 19b₁). XPS Fe 2p, Cr 2p and Ti 2p analysis of the 2–AB samples was conducted as the same condition of the 0-AB sample. For Fe 2p XPS, the signal revealed the presence of Fe_2O_3 and Fe–Cr–O at both Fe $2p_{1/2}$ and Fe $2p_{3/2}$ peaks,
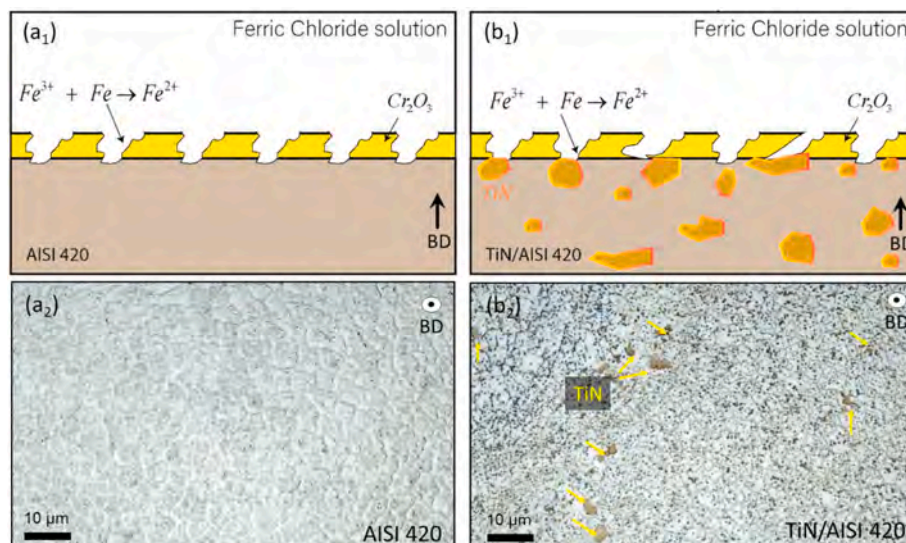

Fig. 19. Indicates (1) the surface morphologies mechanism, and (2) optical images after corrosion time for (a) 0–AB, and (b) 2–AB.
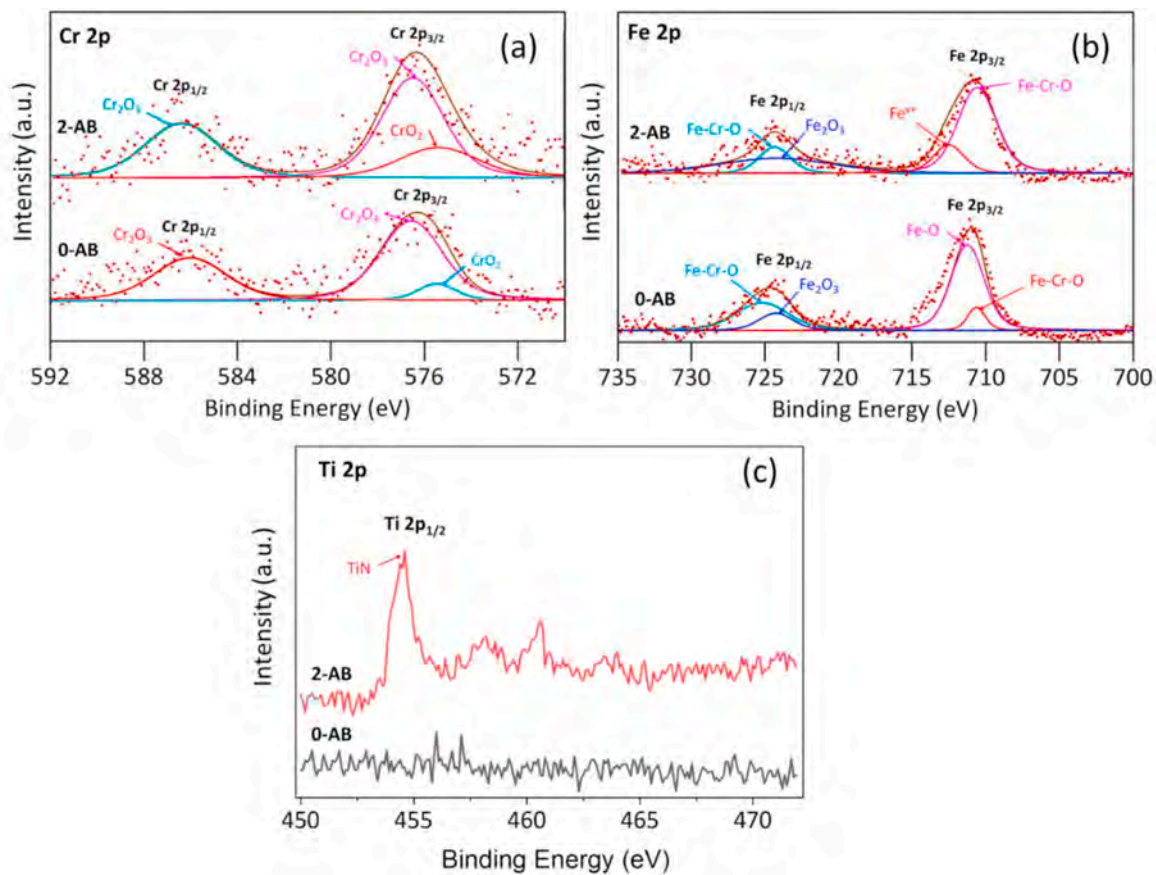
Fig. 20. Illustrates the XPS spectra fitting curves of (a) Fe 2p, (b) Cr 2p and (c) Ti 2p for the corrosive surface of 0-AB and 2-AB samples.

similar to the 0–AB sample's data. However, no difference in the intensity of Cr_2O_3 and CrO_2 peaks was observed between the 0-AB and 2-AB samples, as shown in Fig. 20b. Importantly, the TiN particles played a crucial role as a passive film, effectively protecting the material against corrosion. The distribution and presence of TiN within the AISI 420 matrix were confirmed through an optical image (Fig. 19b$_2$) and by detecting the Ti 2p$_{3/2}$ signal at 454.5 eV for the 2-AB sample (Fig. 20c), referencing research [45]. These XPS observations support the hypothesis that the incorporation of Cr_2O_3 and TiN, contributing the anti-corrosive of the TiN/AISI 420 samples. Consequently, a larger in the content and uniform distribution of TiN within the AISI 420 matrix was noted, significantly enhancing the corrosion resistance of the TiN/AISI 420 samples.

In addition, the austenite phase is acknowledged for providing superior corrosion resistance compared to the Martensitic phase [35]. During the heat treatment process, the Martensite-Austenite transformation took place, leading to an increased presence of the austenite phase in the microstructure and a higher Cr content (Tables 1 and 2 and Fig. 14). This transformation stood as the primary reason for the heightened corrosion resistance observed in the HT samples compared to the AB samples.

5. Conclusions

This study focused on exploring the impact of TiN–x content (x = 0, 0.5, 1, and 2 wt %) and heat treatment on the microstructure, mechanical properties, and corrosion behaviors of the TiN/AISI 420 composites fabricated by the SLM method. The as-built and heat treatment of the SLM TiN/AISI 420 samples are called x–AB and x–HT, respectively. Key findings include.

(1) Higher TiN content in the AISI 420 matrix increased the average grain size in both AB and HT samples, attributed to reduced laser absorption and thermal expansion differences.

(2) In both AB and HT samples, martensite predominated, followed by retained austenite and TiN. Lower TiN content corresponded to higher retained austenite in the matrix, establishing a correlation between TiN phases and its content in the AISI 420 matrix. All HT samples exhibited an increase of retained austenite compared to AB results, establishing a strong correlation with hardness and corrosion resistance.

(3) The optimal hardness, 745 ± 12 H V, was observed in 1–AB samples, attributed to lower grain size (approximately 1.5 μm) and the presence of TiN particles on grain boundaries as a strengthening phase. Elevated surface residual stress could also contribute to increased hardness. Conversely, 2–AB samples exhibited lower hardness than 0–AB, explained by the increased grain size. Heat treatment produced a softening effect on all HT samples due to reduced residual stress.

(4) All AB samples demonstrated higher tensile strength than SLM pure AISI 420, with the 1–AB sample exhibiting the highest tensile strength. Following the post-heat treatment process, a noticeable trend reversal occurred, mirroring hardness changes. All HT samples displayed increased tensile strength and elongation, with maximum values of 1860 ± 36 MPa for strength and 7.3 ± 2 % for elongation observed in the 1–HT samples.

(5) The presence of TiN particles significantly impacted corrosion resistance in AB and HT samples. As TiN content increased, the corrosion resistance of the AB enhanced. Among AB samples, the 2–AB sample demonstrated notable corrosion resistance. Additionally, HT samples exhibited higher corrosion resistance than

AB samples, with the lowest recorded corrosion rate at 104.7 mm/year for 2–HT, representing an improvement in results.

CRediT authorship contribution statement

Duc Tran: Writing – original draft, Methodology, Investigation, Formal analysis, Data curation, Conceptualization. **Chih-Kuang Lin:** Validation, Methodology. **Pi-Cheng Tung:** Validation, Methodology. **Chin-Te Lin:** Validation, Software. **Jeng-Rong Ho:** Writing – review & editing, Validation, Supervision, Resources, Project administration, Funding acquisition, Conceptualization. **Yoshiyuki Iizuka:** Data curation. **I-Yu Tsao:** Data curation. **Thanh-Long Le:** Validation.

Declaration of competing interest

The authors whose names are listed immediately below certify that they have NO affiliations with or involvement in any organization or entity with any financial interest (such as honoraria; educational grants; participation in speakers' bureaus; membership, employment, consultancies, stock ownership, or other equity interest; and expert testimony or patent-licensing arrangements), or non-financial interest (such as personal or professional relationships, affiliations, knowledge or beliefs) in the subject matter or materials discussed in this manuscript.

Data availability

Data will be made available on request.

References

[1] M. Brandt, Laser Additive Manufacturing: Materials, Design, Technologies, and Applications, Elsivier, UK, 2016. Edinbugh.

[2] A. Vafadar, F. Guzzomi, A. Rassau, K. Hayward, Advances in metal additive manufacturing: a review of common processes, industrial applications, and current challenges, Appl. Sci. 11 (3) (Jan 2021). http://10.3390/app11031213.

[3] Y. Tian, K. Chadha, C. Aranas, Laser powder bed fusion of ultra-high-strength 420 stainless steel: microstructure characterization, texture evolution and mechanical properties, Mater. Sci. Eng., A 805 (Feb 2021) 140790, https://doi.org/10.1016/j.msea.2021.140790.

[4] J.M. Jeon, et al., Effects of microstructure and internal defects on mechanical anisotropy and asymmetry of selective laser-melted 316L austenitic stainless steel, Mater. Sci. Eng., A 763 (Aug 2019) 138152, https://doi.org/10.1016/j.msea.2019.138152.

[5] A. Hemmasian Ettefagh, S. Guo, J. Raush, Corrosion performance of additively manufactured stainless steel parts: a review, Addit. Manuf. 37 (Jan 2021) 101689, https://doi.org/10.1016/j.addma.2020.101689.

[6] M.-K. Kim, Selective laser melting of metal matrix composites: a review of materials and process design, Composites Res. 1 (4) (Sep 2021) 221–225.

[7] W. Chen, B. Xiao, L. Xu, Y. Han, L. Zhao, H. Jing, Additive manufacturing of martensitic stainless steel matrix composites with simultaneously enhanced strength-ductility and corrosion resistance, Compos. B Eng. 234 (Apr 2022) 109745. https://doi.org/10.1016/j.compositesb.2022.109745.

[8] C. Gao, Z. Wang, Z. Xiao, D. You, K. Wong, and A. H. Akbarzadeh, "Selective laser melting of TiN nanoparticle-reinforced AlSi10Mg composite: Microstructural, interfacial, and mechanical properties", J. Mater. Process. Technol., Vol. 2812020. DOI: https://doi.org/10.1016/j.jmatprotec.2020.116618.

[9] B. Li, L. Zhang, Y. Xu, Z. Liu, B. Qian, F. Xuan, Selective laser melting of CoCrFeNiMn high entropy alloy powder modified with nano-TiN particles for additive manufacturing and strength enhancement: process, particle behavior and effects, Powder Technol. 360 (Jan 2020) 509–521. https://doi.org/10.1016/j.powtec.2019.10.068.

[10] L. Xi, et al., Interfacial structure and wear properties of selective laser melted Ti/(TiC+TiN) composites with high content of reinforcements, J. Alloys Compd. 870 (Jul 2021) 159436, https://doi.org/10.1016/j.jallcom.2021.159436.

[11] A. Ozsoy, E. Aydogan, and A. F. Dericioglu, "Selective laser melting of Nano-TiN reinforced 17-4 PH stainless steel: Densification, microstructure and mechanical properties", Mater. Sci. Eng., A, Vol. 8362022. DOI: http://10.1016/j.msea.2021.142574.

[12] Q. Tan, et al., Unravelling the roles of TiN-nanoparticle inoculant in additively manufactured 316 stainless steel, J. Mater. Sci. Technol. 175 (March 2024) 153–169, https://doi.org/10.1016/j.jmst.2023.08.018.

[13] J. Zhang, et al., Effect of process parameters and heat treatment on the properties of stainless steel CX fabricated by selective laser melting, J. Alloys Compd. 877 (Oct 2021) 160062, https://doi.org/10.1016/j.jallcom.2021.160062.

[14] S. Chen, et al., Effect of heat treatment on the anisotropy in mechanical properties of selective laser melted AlSi10Mg, Mater. Sci. Eng., A 858 (Nov 2022) 144130, https://doi.org/10.1016/j.msea.2022.144130.

[15] K. Saeidi, et al., Ultra-high strength martensitic 420 stainless steel with high ductility, Addit. Manuf. 29 (Jan 2019) 100803, https://doi.org/10.1016/j.addma.2019.100803.

[16] X. Zhao, Q.S. Wei, N. Gao, E.L. Zheng, Y.S. Shi, S.F. Yang, Rapid fabrication of TiN/AISI 420 stainless steel composite by selective laser melting additive manufacturing, J. Mater. Process. Technol. 270 (Aug 2019) 8–19. https://10.1016/j.jmatprotec.2019.01.028.

[17] D. Tran, et al., Enhancing mechanical and corrosion properties of AISI 420 with titanium-nitride reinforcement through high-power-density selective laser melting using two-stage mixed TiN/AISI 420 powder, Materials 16 (11) (Jun 2023). https://10.3390/ma16114198.

[18] D. Tran, C.-K. Lin, P.-C. Tung, J.-R. Ho, T.-L. Le, Enhancing mechanical properties of selective-laser-melting TiN/AISI 420 composites through Taguchi GRA and PCA multi-response optimization, J. Mater. Res. Technol. 2024/01/20 (2024), https://doi.org/10.1016/j.jmrt.2024.01.174.

[19] Standard Test Methods for Tension Testing of Metallic Materials, ATSM E8/E8M standard, last updated Jul 2022. DOI: http://10.1520/E0008_E0008M-22.

[20] Standard test methods for density of compacted or sintered powder metallurgy (PM) products using Archimedes, Principle, ASTM B962–23 (2023) last updated Sep.

[21] C. Ukpaka, S. Amadi, I. Odharo, Modeling the rate of biocorrosion and the effects of redox-reactions of metals in water environment, J. Eng. Technol. Res. 3 (13) (2011) 371–380.

[22] W.-S. Shin, et al., Heat treatment effect on the microstructure, mechanical properties, and wear behaviors of stainless steel 316L prepared via selective laser melting, Mater. Sci. Eng., A 806 (Mar 2021) 140805, https://doi.org/10.1016/j.msea.2021.140805.

[23] Y. Zhong, L. Liu, S. Wikman, D. Cui, Z. Shen, Intragranular cellular segregation network structure strengthening 316L stainless steel prepared by selective laser melting, J. Nucl. Mater. 470 (2016) 170–178. http://10.1016/j.jnucmat.2015.12.034.

[24] B. Song, S. Dong, C. Coddet, Rapid in situ fabrication of Fe/SiC bulk nanocomposites by selective laser melting directly from a mixed powder of microsized Fe and SiC, Scripta Mater. 75 (Mar 2014) 90–93.

[25] W.-S. Shin et al., "Heat treatment effect on the microstructure, mechanical properties, and wear behaviors of stainless steel 316L prepared via selective laser melting", Mater. Sci. Eng., A, Vol. 8062021. DOI: http://10.1016/j.msea.2021.140805.

[26] J. Liu, et al., Effect of scanning speed on the microstructure and mechanical behavior of 316L stainless steel fabricated by selective laser melting, Mater. Des. 186 (Jan 2020) 108355, https://doi.org/10.1016/j.matdes.2019.108355.

[27] S. Morito, H. Tanaka, R. Konishi, T. Furuhara, T. Maki, The morphology and crystallography of lath martensite in Fe-C alloys, Acta Mater. 51 (6) (Apr 2003) 1789–1799, https://doi.org/10.1016/S1359-6454(02)00577-3.

[28] H. Kitahara, R. Ueji, N. Tsuji, Y. Minamino, Crystallographic features of lath martensite in low-carbon steel, Acta Mater. 54 (5) (Mar 2006) 1279–1288, https://doi.org/10.1016/j.actamat.2005.11.001.

[29] Y. Liu, M. Tang, Q. Hu, Y. Zhang, L. Zhang, Densification behavior, microstructural evolution, and mechanical properties of TiC/AISI420 stainless steel composites fabricated by selective laser melting, Mater. Des. 187 (Feb 2020) 108381. http://10.1016/j.matdes.2019.108381.

[30] Z. Ahmad, Principles of Corrosion Engineering and Corrosion Control, Elsevier, 2006.

[31] C.D. Boley, S.A. Khairallah, A.M. Rubenchik, Calculation of laser absorption by metal powders in additive manufacturing, Appl. Opt. 54 (9) (Mar 2015) 2477–2482. http://10.1364/AO.54.002477.

[32] L. Hadji, Morphological instability prior to particle engulfment by a solidifying interface, Scripta Mater. 48 (6) (Mar 2003) 665–669, https://doi.org/10.1016/S1359-6462(02)00562-6.

[33] K. Arafune, A. Hirata, Thermal and solutal Marangoni convection in In–Ga–Sb system, J. Cryst. Growth 197 (4) (Mar 1999) 811–817, https://doi.org/10.1016/S0022-0248(98)01071-9.

[34] L.Y. Chen, et al., Processing and properties of magnesium containing a dense uniform dispersion of nanoparticles, Nature 528 (7583) (Dec 2015) 539–543. http://10.1038/nature16445.

[35] J. Sander, J. Hufenbach, L. Giebeler, M. Bleckmann, J. Eckert, U.J.S.M. Kühn, Microstructure, Mechanical Behavior, and Wear Properties of FeCrMoVC Steel Prepared by Selective Laser Melting and Casting, vol. 126, 2017, pp. 41–44.

[36] D. Gu, H. Wang, D. Dai, P. Yuan, W. Meiners, R. Poprawe, Rapid fabrication of Al-based bulk-form nanocomposites with novel reinforcement and enhanced performance by selective laser melting, Scripta Mater. 96 (Feb 2015) 25–28, https://doi.org/10.1016/j.scriptamat.2014.10.011.

[37] Y. Qi, Z. Hu, H. Zhang, X. Nie, C. Zhang, H. Zhu, High strength Al–Li alloy development for laser powder bed fusion, Addit. Manuf. 47 (Nov 2021) 102249, https://doi.org/10.1016/j.addma.2021.102249.

[38] W. Chen, L. Xu, Y. Zhang, Y. Han, L. Zhao, H. Jing, Additive manufacturing of high-performance 15-5PH stainless steel matrix composites, Virtual Phys. Prototyp. 17 (2) (Apr 2022) 366–381. https://doi.org/10.1080/17452759.2021.2019793.

[39] A. Pfennig, A. Kranzmann, Understanding the anomalous corrosion behaviour of 17% chromium martensitic stainless steel in laboratory CCS-Environment—a descriptive approach, Cleanroom Technol. 4 (2) (Mar 2022) 239–257. http://10.3390/cleantechnol4020014.

[40] Y. Zhao, C. Wu, S. Zhou, J. Yang, W. Li, L.-C. Zhang, Selective laser melting of Ti-TiN composites: formation mechanism and corrosion behaviour in H2SO4/HCl mixed solution, J. Alloys Compd. 863 (2021) 158721. May, http://10.1016/j.jallcom.2021.158721.

[41] B.J. Tan, K.J. Klabunde, P.M.A. Sherwood, X-ray photoelectron spectroscopy studies of solvated metal atom dispersed catalysts. Monometallic iron and bimetallic iron-cobalt particles on alumina, Chem. Mater. 2 (2) (Mar 1990) 186–191, https://doi.org/10.1021/cm00008a021.

[42] J.C. Langevoort, I. Sutherland, L.J. Hanekamp, P.J. Gellings, On the oxide formation on stainless steels AISI 304 and incoloy 800H investigated with XPS, Appl. Surf. Sci. 28 (2) (Apr 1987) 167–179, https://doi.org/10.1016/0169-4332(87)90062-6.

[43] M. Oku, K. Hirokawa, X-ray photoelectron spectroscopy of Co3O4, Fe3O4, Mn3O4, and related compounds, J. Electron. Spectrosc. Relat. Phenom. 8 (5) (Jan 1976) 475–481, https://doi.org/10.1016/0368-2048(76)80034-5.

[44] E. Paparazzo, XPS and auger spectroscopy studies on mixtures of the oxides SiO2, Al2O3, Fe2O3 and Cr2O3, J. Electron. Spectrosc. Relat. Phenom. 43 (2) (Jan 1987) 97–112, https://doi.org/10.1016/0368-2048(87)80022-1.

[45] M. Kawamura, Y. Abe, H. Yanagisawa, K. Sasaki, Characterization of TiN films prepared by a conventional magnetron sputtering system: influence of nitrogen flow percentage and electrical properties, Thin Solid Films 287 (1) (Oct 1996) 115–119, https://doi.org/10.1016/S0040-6090(96)08749-4.